Hypothesis of two-dimensional stripe arrangement and its implications for the superconductivity in high-T_c cuprates

B. V. Fine*
Max Planck Institute for the Physics of Complex Systems, Noethnitzer Str. 38, D-01187, Dresden, Germany
(Received 12 August 2003; revised manuscript received 14 July 2004; published 7 December 2004)

The hypothesis that holes doped into high-T_c cuprate superconductors organize themselves in two-dimensional (2D) array of diagonal stripes is discussed, and, on the basis of this hypothesis, a new microscopic model of superconductivity is proposed and solved. The model describes two kinds of hole states localized either inside the stripes or in the antiferromagnetic domains between the stripes. The characteristic energy difference between these two kinds of states is identified with the pseudogap. The onset of superconductivity is caused by the interaction, which is assumed to be mediated by the transverse fluctuations of stripes. The superconducting (SC) order parameter predicted by the model has two components, whose quantum phases exhibit a complex dependence on the the center-of-mass coordinate. The model predictions for the tunneling characteristics and for the dependence of the critical temperature (T_c) on the superfluid density show good quantitative agreement with a number of experiments. The model, in particular, predicts that the SC peaks in the tunneling spectra are asymmetric, only when $\Delta/T_c > 4$, where Δ is the SC gap. It is also proposed that, at least in some high-T_c cuprates, there exist two different superconducting states corresponding to the same doping concentration and the same critical temperature. Finally, the checkerboard pattern in the local density of states observed by scanning tunneling microscopy in $Bi_2Sr_2CaCu_2O_{8+\delta}$ is interpreted as coming from the states localized around the centers of stripe elements forming the 2D superstructure.

DOI: 10.1103/PhysRevB.70.224508 PACS number(s): 74.72.−h, 74.20.Mn

I. INTRODUCTION

At present, the school of thought, which stipulates the importance of local inhomogeneous structures called "stripes" for the physics of high-T_c cuprate superconductors, is dominated by the view that stripes form a one-dimensional (1D) array, where each of them runs parallel to one of the principal lattice directions.[1–11] This picture, however, entails a number of difficulties associated with the stripe geometry. In particular, in the presence of stripes parallel to the principal lattice directions, it is difficult to explain why the "nodal" quasiparticles having momentum directed along lattice diagonals (i.e., at 45° with respect to stripes), remain least gapped with the onset of both the pseudogap phenomenon and superconductivity.

In this work, I propose a microscopic model, which is based on the hypothesis that, at those doping concentrations, where superconductivity is observed in high-T_c cuprates, the holes organize themselves into a two-dimensional (2D) array of diagonal stripes. The 2D stripe superstructure does not incur the geometrical difficulties associated with 1D stripe arrays. This superstructure has been mentioned in the literature[1,5,9,11–13] (sometimes under the name of "grid" or "checkerboard"), but a number of experimental and theoretical arguments have been put forward against its existence. However, as I discuss later (in Sec. III), the 2D stripe scenario has not been yet ruled out entirely. At the same time, this scenario has never been analyzed persistently enough, in part, because no theoretical model has been put forward, which would relate the 2D stripe superstructure to superconductivity.

The model proposed in this work reconciles the 2D stripe geometry with superconductivity by demonstrating, that the superconductivity can be carried by states localized in the 2D stripe background. The interaction, which, in the model, leads to the superconducting (SC) transition, is, presumably, mediated by the transverse fluctuations of stripes.

The picture emerging in the framework of the 2D diagonal stripe hypothesis also offers a very simple interpretation of the pseudogap phenomenon,[14–17] including its role in the superconductivity of cuprates. Other experimental facts to be interpreted in this work are: (i) quasiparticle coherence in *k*-space, which emerges only below the SC transition; (ii) the asymmetry in the tunneling density of states; (iii) linear density of states in the vicinity of the chemical potential; (iii) the checkerboard pattern in the local density of states in $Bi_2Sr_2CaCu_2O_{8+\delta}$ (Bi-2212) observed by scanning tunneling microscopy (STM)[18–21] (iv) low superfluid density and the universal dependence thereof on the critical temperature.

The SC order parameter obtained in this work has complex two-component structure, which cannot be described as either *s*-wave or *d*-wave or the combination of two. The distinctive unconventional feature of this order parameter is the nontrivial symmetry with respect to spatial translations, which includes the sign change of at least one of the two components.

Reviewing the relevant literature, it should be noted that the general idea of superconductivity carried by localized states has been discussed in the past in the context of various physical systems including high-T_c cuprates.[22–26] At a different level, this work also contains parallels with several theoretical proposals,[27–29] which involve two-component scenarios for high-T_c cuprates. Since the 2D stripe superstructure can be viewed as a collection of nanodomains having different electronic properties, the present work can be linked to a more general class of ideas stipulating some

kind of phase separation in cuprates (see, e.g., Ref. 30). If only the charge ordering associated with the 2D stripe superstructure is considered, then it exhibits certain similarities with Wigner crystals advocated in some of more recent proposals.[31,32]

The rest of the paper is organized as follows: In Sec. II the hypothesis of 2D diagonal stripe configuration is formulated. In Sec. III, the arguments in favor and against the existence of such a configuration are discussed. Possible dynamic properties of this configuration are briefly analyzed in Sec. IV. In Sec. V, the properties of hole excitations in the presence of the 2D stripe configuration are described, and the pseudogap phenomenon is identified. In Sec. VI, a model describing the hole excitations in the stripe background is formulated and solved in the mean-field approximation. In Sec. VII, the realistic features of the model and the resulting phase diagram are discussed. The model predictions are compared with experiments in Sec. VIII.

This paper is quite long, in part, because some of the model predictions tested in Sec. VIII require detailed calculations. In the first reading, one can, therefore, review all the figures in the theoretical sections, read Sec. VI A, and then proceed with reading Sec. VIII.

II. TWO-DIMENSIONAL CONFIGURATION OF DIAGONAL STRIPES

In this section, I introduce the basic assumption of the present work, namely, the two-dimensional configuration of energetically deep and spatially narrow stripes.

I assume that, at sufficiently high doping concentrations, high-T_c cuprates find it energetically favorable to organize the spins of copper atoms into the background of antiferromagnetic (AF) domains as shown in Fig. 1(a). Such a background creates an effective potential for the holes with minimum at the boundaries between those domains.[33] Indeed, if one considers only the nearest neighbor exchange interaction between spins, then placing a hole in the middle of an AF domain would cost energy $4J$, whereas at the domain boundary it costs $0J$. (Here J is the nearest neighbor exchange coupling constant.) The hole kinetic energy at the boundary is also lower than inside an AF domain, because in the latter case, the hole cannot hop to the neighboring sites without increasing the exchange energy of the system, while, in the former case, it can. I further assume that the gain in the exchange and the kinetic energies outweighs the loss in the Coulomb energy (associated with the repulsion between holes). Therefore, holes fill the domain boundaries and thus form stripes [see Figs. 1(b) and 1(c)]. It is not important for the present work whether stripes are centered on copper atoms, as shown in Figs. 1(b) and 1(c), or on oxygen atoms (i.e., on the "bonds" between copper sites).

The AF domains formed between the stripes fall in two groups, which can be distinguished by the value of an AF index η (+1 or −1) representing the sign of the AF order parameter within a given domain. It is easy to see in Figs. 1(a)–1(c), that the AF indices η of two neighboring AF domains always have opposite signs.

A few mathematical facts about this kind of superlattice:

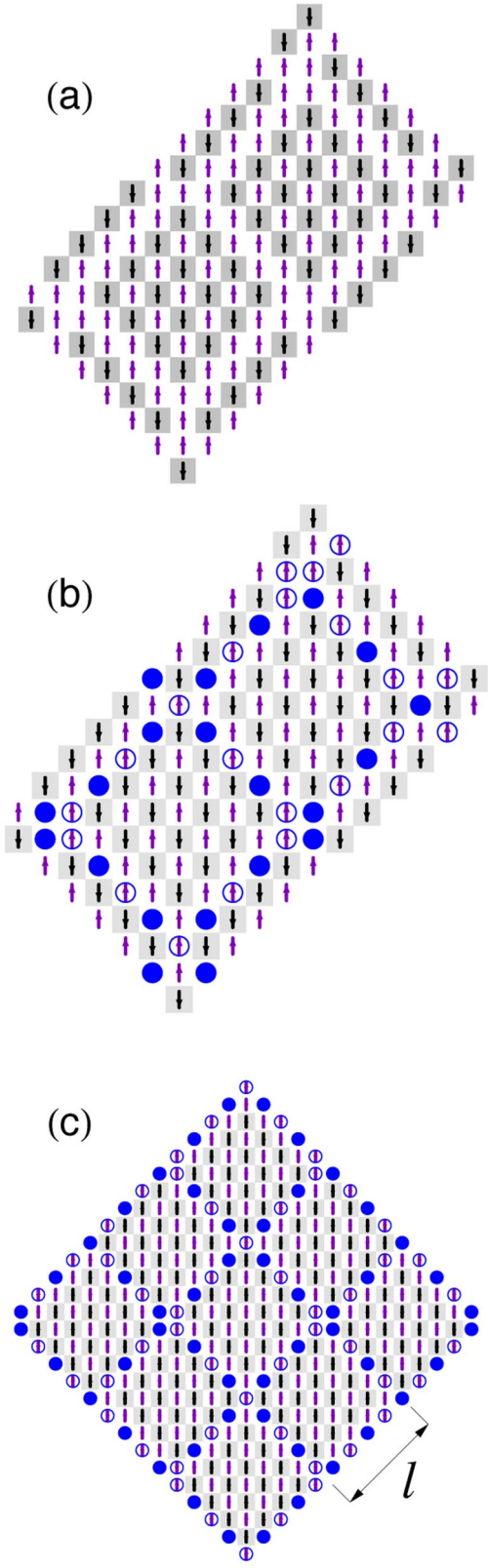

FIG. 1. (Color online) 2D configuration of diagonal stripes: (a) Stripes in spin structure isolating two AF domains with opposite sign of AF vector. (b) The same as (a) but with holes (filled circles) occupying every second site along the spin stripes. Spins on the remaining stripe sites are circled to guide the eye. (c) The same as (b) but with more stripe supercells shown.

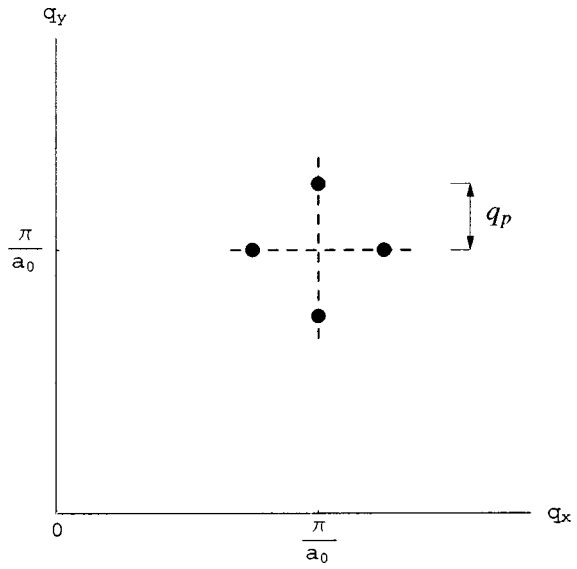

FIG. 2. Fourfold splitting of magnetic inelastic neutron scattering peak.

The spin periodicity of such a structure along each of the two diagonal directions is 2ℓ, where ℓ is the side length of a single AF domain.

For such a structure, the main splitting of the magnetic inelastic neutron scattering (INS) peak around the AF wave vector $\left(\frac{\pi}{a_0};\frac{\pi}{a_0}\right)$ is expected to be fourfold as shown in Fig. 2. (Here a_0 is the lattice period.) The characteristic wave vector q_p of this splitting is frequently parametrized as

$$q_p = \frac{2\pi}{a_0}\delta, \tag{1}$$

where, in the present case

$$\delta = \frac{a_0}{\ell\sqrt{2}}. \tag{2}$$

Theoretically, there should also exist other peaks corresponding to the higher order Fourier harmonics of the stripe superstructure.

Neglecting the intersections between stripes, the fraction of lattice sites lying on the stripes is

$$f = \frac{a_0\sqrt{2}}{\ell} = 2\delta. \tag{3}$$

The assumption of energetically deep stripes made earlier implies that most holes are located inside the stripes. In this case, the fraction of stripe sites occupied by holes is

$$c = \frac{x_d}{f} = \frac{x_d}{2\delta}, \tag{4}$$

where x_d is the dimensionless doping concentration.

Yamada *et al.*[34] have discovered experimentally that in underdoped $La_{2-x}Sr_xCuO_4$ (LSCO)

$$\delta \approx x_d, \tag{5}$$

which means that $c \approx \frac{1}{2}$, or the hole content of diagonal stripes can be set empirically at 1 hole per two stripe sites (the same as 1 hole per length $2a_0\sqrt{2}$).

Below, I will use the term "stripe element" to refer to the part of a stripe which constitutes a side of one AF domain. On the basis of empirical relation (5), I can estimate the number of lattice sites in one stripe element as

$$\frac{\ell}{a_0\sqrt{2}} = \frac{1}{2x_d}. \tag{6}$$

Doping concentration $x_d = 1/8$, taken as an example, then corresponds to $\ell = 4a_0\sqrt{2}$.

III. ARGUMENTS IN FAVOR AND AGAINST THE EXISTENCE OF THE 2D DIAGONAL STRIPE STRUCTURE

If stripes exist, then the primary evidence for their geometrical properties comes from the fourfold splitting of the magnetic INS peak [usually called the (π,π) peak], which was described in the previous section and shown in Fig. 2. This splitting was observed in the underdoped compounds of LSCO[34] and $YBa_2Cu_3O_{6+x}$ (YBCO)[35–37] families of high-T_c superconductors.

A straightforward interpretation of this peak pattern is that the antiferromagnetic spin structure $\cos\left(\frac{\pi}{a_0}x\right)\cdot\cos\left(\frac{\pi}{a_0}y\right)$ is modulated along both diagonal directions by function $\cos\left[\frac{\pi\delta}{a_0}(x+y)\right]\cos\left[\frac{\pi\delta}{a_0}(x-y)\right]$. (Coordinates x and y correspond, respectively, to the horizontal and vertical axes in Figs. 1(a)–1(c).) The modulation function can then be expanded as the sum $\frac{1}{4}[e^{i2\pi\delta x/a_0}+e^{-i2\pi\delta x/a_0}+e^{i2\pi\delta y/a_0}+e^{-i2\pi\delta y/a_0}]$—hence the fourfold splitting of the main peak.

However, since the early indications of the stripe nature of the (π,π) peak splitting,[8] most of the "stripe community" has opted for an interpretation of experiments in terms of the superposition of two two-peak splittings. The two kinds of splitting were described as coming from two kinds of spatially separated domains—each representing a one-dimensional array of stripes running along one of the principal lattice directions.

There, indeed, exist a number of theories[1–7] suggesting that stripes extending along the principal lattice directions are more favorable energetically than diagonal stripes. (The 2D diagonal stripe superstructure has been explicitly considered, e.g., in Refs. 1, 5, and 12.) This is, however, a delicate energetic balance, which should be sensitive to numerous factors, not all of which are taken into account by the above-mentioned theories. For example, the interaction with the crystal lattice and the long-range Coulomb interaction are, typically, neglected in the numerical studies, even though the energy associated with each of these two interactions can change the outcome of the competition between different stripe configurations. Since the chances of bringing the stripe energetics under the full control of first principles calculations are quite slim, the choice between different stripe configurations (including the absence of stripes) should be made, eventually, on the basis of experiments.

On the experimental side, one can find three main observations suggesting the one-dimensional nature of the stripe pattern.[11]

First, in other materials structurally similar to high-T_c superconducting cuprates, such as, e.g., insulating $La_{1.95}Sr_{0.05}CuO_4$[38] and nickelate $La_{2-x}Sr_xNiO_{4+y}$,[39,40] there exists direct experimental evidence of the 1D nature of stripe modulations.

Second, the two-dimensional spin structure modulation of the form $\cos\left[\frac{\pi\delta}{a_0}(x+y)\right]\cos\left[\frac{\pi\delta}{a_0}(x-y)\right]$ should induce an effective potential for electric charge roughly of the form $\left\{\cos\left[\frac{\pi\delta}{a_0}(x+y)\right]\cos\left[\frac{\pi\delta}{a_0}(x-y)\right]\right\}^2$. If the spin modulation is weak, then it follows from the Landau theory of the second order phase transitions[13,41] that the peak structure for the charge inelastic neutron scattering corresponding to the above potential should exhibit four main peaks around (0,0). The orientation of these peaks should be rotated by 45° with respect to the splitting of the magnetic peak, and characterized by the separation $\frac{2\pi}{a_0}\delta\sqrt{2}$ from (0,0). The argument against the diagonal 2D spin stripes is that the above charge peaks have not been observed, while the charge peaks expected for the 1D superstructure were observed.[13]

Finally, the third and, perhaps, the most direct experimental observation suggesting the one-dimensionality of the stripe superstructure comes from Ref. 9 (also supported by Ref. 42), where it was found that partial detwinning of a YBCO sample leads to a very strong asymmetry of the (π,π) peak splitting. This asymmetry is in quantitative agreement with the expectation that each of the twin domains in YBCO has only one kind of one-dimensional stripe pattern, and, therefore, partial detwinning should lead to a significant redistribution of intensities between the four peaks.

The arguments counterbalancing the above experimental observations can be the following:

The first observation, although important, is only indirect and thus cannot substitute for direct observations.

The interpretation of the second observation is based on the assumption that the spin structure is weakly modulated by function $\cos\left[\frac{\pi\delta}{a_0}(x+y)\right]\cos\left[\frac{\pi\delta}{a_0}(x-y)\right]$. As a result the charge modulation is also assumed to be small, and, therefore, the Landau theory is applied. However, if the modulation of the the AF structure is strong, and the stripes are, indeed, deep and narrow as assumed in Sec. II, then the four charge peaks proposed as an indicator of the 2D nature of stripe pattern would only be a part of a more complicated peak structure, and not necessarily the most pronounced one. For example, for a more realistic charge profile modulated as $\cos^8\left[\frac{\pi\delta}{a_0}(x+y)\right]\sin^2\left[\frac{\pi\delta}{a_0}(x-y)\right]+\sin^2\left[\frac{\pi\delta}{a_0}(x+y)\right]\cos^8\left[\frac{\pi\delta}{a_0}(x-y)\right]$, the positions of the strongest satellite peaks coincide with those expected for the 1D picture.

The effect of the 45° rotation of some modulation peaks can, nevertheless, be relevant in another context. It will be shown in Sec. VIII C, that this effect can lead to the checkerboard pattern observed by STM in the local density of states of Bi2212.[18–20]

Concerning the third argument against the 2D diagonal stripe picture, the experimental data, as they stand, appear quite convincing. Yet, this kind of evidence has been limited so far only to YBCO. The significant internal anisotropy of the lattice structure in YBCO can, in principle, induce an anisotropic INS response even of a truly two-dimensional stripe superstructure. Thus the final resolution of the dilemma between 2D structure with anisotropic properties and a 1D structure cannot be relied on this experiment alone. [Later note: A very recent INS study[43] has shown that the splitting of the (π,π) peak measured on *detwinned* YBCO crystals is anisotropic but clearly two-dimensional.]

IV. DYNAMIC PROPERTIES OF THE STRIPE STRUCTURE

Now I address the question, to what extent the stripe picture described in Sec. II can possess dynamic properties.

There are two possibilities for the time dependence of that structure.

The first possibility is that the stripe boundaries of AF domains can fluctuate and then drift away. One circumstance that favors the fluctuations of stripes with or without average drift is that, in the approximation of the nearest neighbor exchange and without holes placed inside the stripes, the spins located on the diagonal boundaries of AF domains have zero exchange energy and thus are free to flip [see Fig. 1(a)]. This would not be the case if the AF domain boundaries were oriented along the principal lattice directions.

With holes inside the stripes, it is even easier for the stripes to fluctuate locally, but it is more difficult to drift on average. The Coulomb repulsion between different stripe elements, the topology of the 2D stripe superstructure and pinning on impurities and structural disorder should inhibit the average drift of the stripe pattern.

Thus, in the following, I will assume that, on the time scales relevant to the physics of superconductivity, the stripe superstructure does not drift, even though individual stripe elements may exhibit strong transverse fluctuations.

The second possibility for the time dependence of the stripe superstructure is that the AF order parameter of a given AF domain can fluctuate and then, perhaps, exhibit "rotational diffusion." The relative spin orientation of neighboring AF domains is fixed not by direct exchange interaction but by the overall energy balance of the entire structure, which does not allow holes to leave the stripes. Spins of a single AF domain cannot simply flip by 180°, because such a flip would dissolve the domain boundaries, which, in turn, would contradict to the assumption that the high energy balance favors the stripe structure. It can, however, happen that the AF order parameter of a given domain fluctuates slightly away from the the anti-alignment orientation with respect to the neighboring domains, and then either this fluctuation is damped back to the initial orientation, or, on the contrary, the neighboring supercells adjust the orientation of their spins, and, in this way, the average orientation of the spin order diffuses away for relatively large regions of the sample. The range of the spin orientations swept by the rotational diffusion will, eventually, depend on the relative strength of the local anisotropy interaction with respect to the the spin fluctuations.

As a consequence of the above kind of rotational diffusion, the elastic response from the modulated AF spin struc-

ture should be either unobservable or strongly suppressed. At the same time, I assume that this diffusion is slow enough and thus can be neglected in a theoretical model of superconductivity. (To date, the elastic response of presumed stripe superstructure has been detected from the superconducting samples of Nd-doped,[8,44] Zn-doped[45–47] and "pure" LSCO[46] and from $La_{1.875}Ba_{0.125-x}Sr_xCuO_4$, see Ref. 48.)

V. POTENTIAL PROFILE AND THE TWO KINDS OF HOLE STATES

The potential profile for the hole excitations in the background of 2D stripe superstructure is sketched in Fig. 3. This profile consists of two main components: the network of narrow potential wells running along the stripes and the (repulsive) Coulomb potential created around them.

It is clear from the above picture, that there are two kinds of hole states: those localized mainly inside the stripes—I will call them *b*-states—and those localized mainly in the shallow potential wells inside the AF domains—I will call them *a*-states.

It is particularly easy to discuss the situation when (A) the in-stripe potential wells are deep enough, so that, at low temperatures, almost all holes stay inside the stripes, and (B) the AF domains are large enough, so that the energy levels of both *a*-states and *b*-states are spaced closely enough, as shown in Fig. 3(c). In this case, the chemical potential μ of holes is approximately equal to the highest energy of occupied *b*-state at zero temperature. This energy should be below E_K [the minimal energy of *a*-states indicated in Fig. 3(c)], which is a formal restatement of the assumption that the stripes are deep.

Such a situation may well correspond to strongly underdoped (but superconducting) cuprates, in which case, the difference $E_K-\mu$ can be identified with the pseudogap defined as the leading-edge midpoint in angle-resolved photoemission spectroscopy.[17] The phenomenology of the pseudogap can then be interpreted as follows. At energies between μ and $E_K-\mu$, the density of states is low, because only *b*-states contribute to this energy range. Moreover, since *b*-states are extended along the diagonal stripes, the momentum of photoelectrons emitted from *b*-states should be preferentially oriented along the lattice diagonals. Above the pseudogap, the density of states gradually increases due to the contribution from *a*-states. The characteristic energy scale of this increase can be estimated as $0.1-0.2$ eV [a typical height of the Coulomb potential barrier E_M-E_K shown in Fig. 3(c)].

If the assumptions (A) and (B) hold at higher doping concentrations, then one can envision some critical concentration (perhaps, not far from the optimal doping), at which the pseudogap measured as $E_K-\mu$ becomes equal to zero. However, the other measure of the pseudogap, the gradual increase of the density of states above $E_K=\mu$, will not disappear as long as stripes remain stable and, therefore, generate locally inhomogeneous Coulomb potential landscape.

One should note, however, that the validity of assumption (B) above is particularly questionable at the doping concentrations corresponding to the physically interesting sizes of AF domains of the order $\ell=4a_0\sqrt{2}\approx 23$ Å (for $a_0=4$ Å). If,

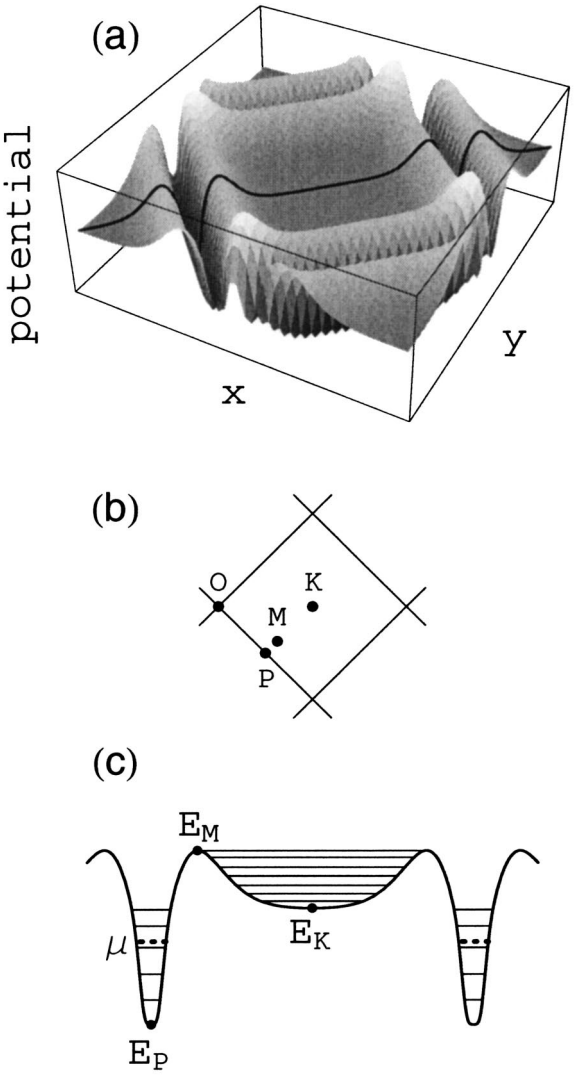

FIG. 3. (a) Sketch of potential landscape within one stripe supercell. (b) Scheme of a stripe supercell. (c) Sketch of potential landscape along the thick line drawn across plot (a). Energies E_K, E_M and E_P correspond to points *K*, *M* and *P* marked in figure (b). Solid horizontal lines indicate quantum levels inside the respective potential wells. Dashed line indicates the position of chemical potential μ.

for an estimate of the level spacing of both *a*- and *b*-states, one takes the spacing between the lowest levels of a free particle having effective mass $m_e^*=5m_e$ in a box of size ℓ, then one obtains 40 meV. (Here m_e is the bare electron mass.) The number 40 meV is of the order of the experimental values of the pseudogap and also notably larger than a typical critical temperature ($\approx$7 meV).

If the level spacing is, indeed, as large as estimated above, then it is likely that there are no states (or very few due to disorder) in the energy range between the highest occupied *b*-state and the lowest *a*-state. In such a case, the position of the chemical potential within the above energy window becomes uncertain. However, the pseudogap can still be de-

fined as $\varepsilon_a - \varepsilon_b$, where ε_a is the lowest energy of *a*-states, and ε_b the energy of a *b*-state closest to the chemical potential.

Formally speaking, the latter definition extends to a somewhat counterintuitive situation characterized by inequality $\varepsilon_a < \varepsilon_b$. While in the underdoped cuprates the strong expectation is that $\varepsilon_a > \varepsilon_b$ for both large and small values of the level spacing, the analysis of experiments in Sec. VIII D will suggest that inequality $\varepsilon_a < \varepsilon_b$ may characterize high-T_c cuprates having doping concentrations above $x_{dC} \approx 0.19$. The condition $\varepsilon_a < \varepsilon_b$ contradicts to the assumption (A) made above. However, as long as there are only a few *a*-states with energies smaller than ε_b, a significant fraction of holes will still be localized inside the stripes and generate the Coulomb potential required for the validity of the sketch shown in Figs. 3(a) and 3(c).

One should also note that the condition $\varepsilon_a < \varepsilon_b$ is detrimental to stripe stability, because it implies that holes penetrate inside AF domains. However, the emergence or disappearance of stripes is not just the subject of one-particle considerations. This process is governed by the balance of global energy, which, among others, includes the contributions from lattice strain and quantum AF fluctuations. It is, therefore, not necessary, and, in fact, unlikely, that stripes become unstable precisely when $\varepsilon_a = \varepsilon_b$. Furthermore, in the present work, the condition $\varepsilon_a < \varepsilon_b$ will only imply one filled *a*-state per AF domain, which the stripe superstructure may, indeed, sustain.

Now I motivate the form of the model Hamiltonian, which will be introduced in the next section.

Describing *b*-states, I assume that they are fermionic states carrying charge *e* and belonging to one stripe element. It will only be important for the model that *b*-states can form pairs with total spin 0. Whether or not they carry spin $1/2$ is not of primary importance.

An *a*-state is the state of one hole injected into a finite AF domain. It is not important for the model to know exactly the orbital and the spin wave functions of *a*-states. It is, however, important to note that (i) the spin wave function of an *a*-state should be fixed by the AF background, which is assumed to be static on the time scale of interest, and (ii) the AF order parameter has opposite signs for two neighboring AF domains. Therefore, if two orbitally equivalent *a*-states from neighboring AF domains form a pair, then the total spin of that pair is equal to zero.

It should be mentioned here that the analogs of *a* and *b*-states have been identified in the numerical study of spin polarons in the stripe background.[33]

As discussed in Sec. IV, the diagonal orientation of stripes predisposes them to strong transverse fluctuations. These fluctuations should, in turn, strongly interact with both *a*- and *b*-states. The effect of this interaction is then twofold. On the one hand, the stripe fluctuations couple to holes both elastically and inelastically, and thus suppress the hole transport across the stripe superstructure. On the other hand, they can efficiently mediate the interaction between different hole states.

The first effect justifies the following "center-of-mass" selection rule: *The model Hamiltonian can have transition elements only between quantum states having the same center-of-mass coordinate*.

This selection rule, first of all, eliminates the direct hopping terms between *a*- and *b*-states belonging to different AF domains or stripe elements. Since this is quite a radical assumption, here I list several additional factors, which contribute to the suppression of hopping in addition to the stripe fluctuations. These factors are: (i) mismatch of AF backgrounds between two neighboring AF domains; (ii) Coulomb potential barriers between neighboring AF domains and between intersecting stripe elements; (iii) disorder in the stripe superstructure (which is not present in Fig. 3 but should be present in a real system). For the subsequent treatment, it is not important, whether *a*- and *b*-states are rigorously localized. All the above factors together should only ensure that the hopping terms are small in comparison with the interaction term discussed below.

In the absence of hopping, every *a*-state and every *b*-state are to be characterized by "on-site" energies ε_a and ε_b, respectively.

I assume that diagonal interactions involving *a*- and *b*-states, and also nondiagonal interactions between *a*-states inside the same AF domain and between *b*-states inside the same stripe element can be satisfactorily taken into account by the renormalization of energies ε_a and ε_b.

Considering the alternatives for nondiagonal interaction terms, I limit the model choices only to the terms of the fourth order with respect to the fermionic creation and annihilation operators. Most of these terms fail to qualify under the center-of-mass selection rule. Among the few terms, which qualify, the only one which will be included in the model corresponds to the transition of two holes occupying two *a*-states *on the opposite sides* of a given stripe element into two *b*-states inside that stripe element and *vice versa* [see Fig. 4(b)]. One can check that the center of mass of two "initial" *a*-states coincides with the center of the stripe element between them, and thus coincides with the center of mass of two "final" *b*-states.

The above transition can be efficiently mediated by the fluctuating stripe element itself. The relevant mechanism would involve two steps. *Step 1:* A hole hops between two adjacent *a*- and *b*-states. Since the two states have different centers of mass, the transition between them should be accompanied by a virtual excitation of the transverse oscillation mode of the stripe element "housing" the *b*-state. *Step 2:* The above oscillation mode is absorbed in the course of the symmetric transition of a second hole, which involves an *a*-state from the other side of the same stripe element and, therefore, restores the center-of-mass position. In order to appreciate this mechanism, one can look at Fig. 3(c), and imagine that, in the course of a transverse fluctuation, one of the two potential wells, which represent stripes, shifts towards the center of the figure. As a result of this shift, the wave function of an *a*-state in the center of the figure strongly overlaps with the wave function of a *b*-state inside the shifted stripe. Such a strong overlap constitutes a precondition for a large value of the interaction term selected for the model.

The above term, which can be schematically described as "$aa \leftrightarrow bb$," is sufficient to achieve the primary goal of the present work, which is to find at least one plausible channel

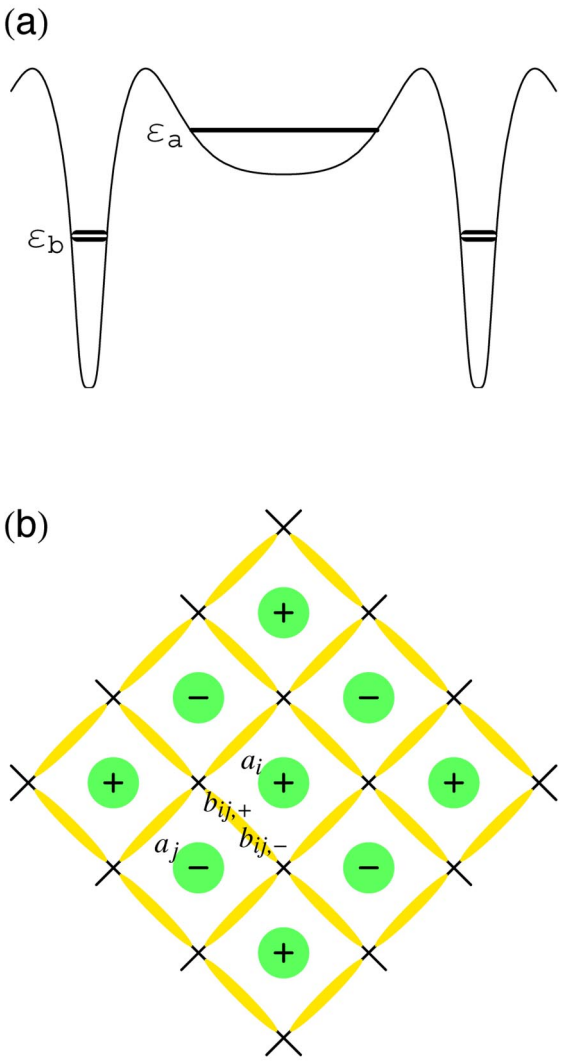

FIG. 4. (Color online) (a) Model quantum states: one a state with energy ε_a inside every AF domain, and two degenerate b-states with energy ε_b inside every stripe element. This picture is to be compared with Fig. 1(c). (b) Two-dimensional scheme of a-states and b-states. Each circle represents the center of an a-state, while each ellipsoid extended along the stripe boundaries represents the location of two b-states. Signs "+" or "−" inside the circles indicate the sign of AF index η_i. Also shown: two operators of a-states and two operators of b-states in their respective spatial domains. The transition between these two pairs of a-states and b-states represents a typical term in the interaction part of Hamiltonian (7).

for the superconductivity in the presence of the 2D arrangement of diagonal stripes. There exist, however, a few other fourth order nondiagonal terms having form "$ab \leftrightarrow ab$", "$aa \leftrightarrow aa$," or "$bb \leftrightarrow bb$," which qualify under the center-of-mass selection rule. At the moment, I rank these terms as less important, because either they involve states, which are too far separated from each other, or they imply no charge flow between different components of the stripe superstructure. Nevertheless, the effect of including additional nondiagonal (and also diagonal) terms in the Hamiltonian would merit further study.

VI. SUPERCONDUCTIVITY MODEL

A. Hamiltonian

In this section, I introduce a model which is minimally sufficient to capture all the elements of the qualitative description given in Sec. V.

The model is limited to the two-dimensional superlattice of a- and b-states, which is shown in Fig. 4. This superlattice is divided into diamond-shaped supercells, like the one shown in Fig. 3(b). The supercells are labeled by single index i (or j). Each of them is characterized by the AF index η_i (defined in Sec. II but now with subscript i). I will use the terms "even supercell" and "odd supercell" to refer to the supercells having $\eta_i=1$ and $\eta_i=-1$, respectively. The total (macroscopic) number of supercells in the system is denoted by variable N. I will further assume that the system has rectangular form of dimensions L_x and L_y along the x- and the y-directions, respectively.

In the present model, there exists only one a-state inside each supercell described by hole annihilation and creation operators a_i and a_i^+, respectively. Each a-state is characterized by the on-site energy ε_a. In order to implement the observation made in the previous section that orbitally equivalent a-states from the neighboring supercells have opposite spins, the spins of a-states alternate together with the AF index η_i, i.e., the spin of ith a-state is equal to $\frac{1}{2}\eta_i$. Operators a_i do not need an additional spin index, because, in this model, the spin of an a-state is not an independent quantum number but instead fixed by the lattice index i.

The next assumption is that, inside each stripe element separating the ith and the jth neighboring supercells, there exist only two b-states both characterized by the same on-site energy ε_b but having different spins ($+1/2$ or $-1/2$). The hole annihilation and creation operators for these states are $b_{ij,\sigma}$ and $b_{ij,\sigma}^+$, respectively. Here index σ represents the spin of a b-state and assumes values $+$ and $-$. (The assumption of a well defined spin is made just for the concreteness of the model. In reality, it can, indeed, be spin but also any other quantum number.)

In total, this model contains one a-state and four b-states per one supercell (two b-states per stripe element times two stripe elements per supercell).

The on-site energies ε_a (the same for all a-states) and ε_b (the same for all b-states) are both measured from the chemical potential. More detailed assumptions about their values will be made later.

Finally, the model Hamiltonian is

$$\mathcal{H} = \varepsilon_a \sum_i a_i^+ a_i + \varepsilon_b \sum_{i,j(i),\sigma}^{\eta_i=1} b_{ij,\sigma}^+ b_{ij,\sigma} + g \sum_{i,j(i)}^{\eta_i=1} (b_{ij,+}^+ b_{ij,-}^+ a_i a_j + \text{h.c.}), \tag{7}$$

where g is the interaction constant. Here and below the notation $j(i)$ in the sum subscript implies that the sum over index j extends only over the nearest neighbors of the ith supercell. Expression $\eta_i=1$ in the sum superscript means that the summation over index i includes only even supercells [marked by pluses in Fig. 4(b)].

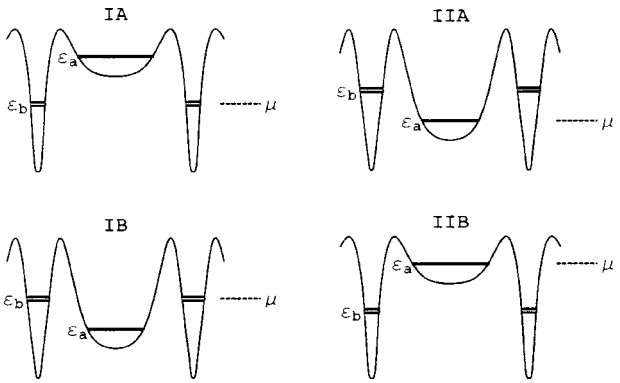

FIG. 5. Sketches representing Cases IA, IB, IIA and IIB.

Hamiltonian (7) can be described as an exotic two-band model, where the noninteracting states are localized but still have the same on-site energy, and the interaction includes only interband coupling. In such a model, the variational SC ground state exists independently of the sign of the coupling constant g. In the calculations, I will, therefore, assume that $g>0$.

Two b-states per stripe element and one a-state per AF domain represent the minimal configuration required for implementing the interaction term in the Hamiltonian (7). At the same time, it should be noted here that the ratio "one hole per $2a_0\sqrt{2}$" extracted in Sec. II from the scaling of INS data also corresponds to two holes per stripe element in the most interesting case of $\ell \approx 4a_0\sqrt{2}$. Furthermore, if the level spacing inside AF domains is, indeed, as large as estimated in Sec. V, then keeping only one a-state per AF domain also constitutes a meaningful approximation for the description of low-energy properties of the system.

B. Classification of the model regimes

The present work is mostly limited to the analytical results describing the following regimes:

Case IA: $\varepsilon_a \geqslant 0$, $\varepsilon_b = 0$,
Case IB: $\varepsilon_a \leqslant 0$, $\varepsilon_b = 0$,
Case IIA: $\varepsilon_a = 0$, $\varepsilon_b \geqslant 0$,
Case IIB: $\varepsilon_a = 0$, $\varepsilon_b \leqslant 0$,
Critical case: $\varepsilon_a = \varepsilon_b = 0$.

The diagrams of energy levels representing Cases IA, IB, IIA, and IIB are sketched in Fig. 5. The reasons for distinguishing those special regimes from the general case ($\varepsilon_a \neq 0, \varepsilon_b \neq 0$) are the following: (i) As shown later in subsection VI D, for the fixed difference $\varepsilon_a - \varepsilon_b$, the situations, when either ε_a or ε_b coincides with the chemical potential (i.e., equal to zero), correspond to sharp minima in the ground state energy. (ii) The condition $\varepsilon_a = 0$ or $\varepsilon_b = 0$ leads to a significant simplification of the model calculations.

Since most observables characterizing Cases IA and IB are identical, these two Cases will be referred to as Case I, whenever the difference between IA and IB is not important. Similarly, "Case II" will refer simultaneously to Cases IIA and IIB.

C. Mean-field solution

In this subsection I shall proceed with finding the variational ground state using the method of Bogoliubov transformation. The variational procedure will consist of (i) making Bogoliubov transformation for b-states in real space; (ii) truncating the Hamiltonian (7) by leaving only the diagonal terms with respect to the new Bogoliubov quasiparticles and then averaging those terms; (iii) making the Fourier transform of a-states; (iv) introducing the Bogoliubov transformation of a-states in k-space; and, finally, (v) minimizing the energy with respect to the both transformations. Although straightforward, the above procedure is somewhat involved. For this reason, in Appendix A, I also present an approximate version of the same mean-field solution. The content of Appendix A also reveals a number of interesting facts about the robustness of the full solution.

The first step of the variational scheme consists of the following Bogoliubov transformation:

$$b_{ij+} = sB_{ij+} + we^{i\varphi_{ij}}B^{+}_{ij-}, \tag{8}$$

$$b_{ij-} = sB_{ij-} - we^{i\varphi_{ij}}B^{+}_{ij+}, \tag{9}$$

where $B_{ij,\sigma}$ are the annihilation operators of the Bogoliubov quasiparticles, s and w are the (real) transformation coefficients satisfying the normalization constraint

$$s^2 + w^2 = 1 \tag{10}$$

and φ_{ij} are the transformation phases chosen to be the same for all translationally equivalent stripe elements.

There exist four translationally nonequivalent types of stripe elements. Each type corresponds to one of the four possible orientations of vector $\mathbf{r}_j - \mathbf{r}_i$, where $\mathbf{r}_i$ and $\mathbf{r}_j$ are the positions of the centers of two neighboring supercells. One of these two supercells is always even, while the other one is always odd. I will use the convention assigning $\mathbf{r}_i$ to an even supercell, and $\mathbf{r}_j$ to an odd one. The four possible realizations of vector $\mathbf{r}_j - \mathbf{r}_i$ are

$$\mathbf{R}_1 = \frac{\ell}{\sqrt{2}}(1,1), \tag{11}$$

$$\mathbf{R}_2 = \frac{\ell}{\sqrt{2}}(-1,1), \tag{12}$$

$$\mathbf{R}_3 = \frac{\ell}{\sqrt{2}}(-1,-1), \tag{13}$$

$$\mathbf{R}_4 = \frac{\ell}{\sqrt{2}}(1,-1). \tag{14}$$

Phases φ_{ij} can now be presented as

$$\varphi_{ij} = \varphi(\mathbf{r}_j - \mathbf{r}_i). \tag{15}$$

They can have, at most, four different values $\varphi_1 = \varphi(\mathbf{R}_1)$, $\varphi_2 = \varphi(\mathbf{R}_2)$, $\varphi_3 = \varphi(\mathbf{R}_3)$ and $\varphi_4 = \varphi(\mathbf{R}_4)$. I label these four phases by index α and refer to them using the notation

$$\varphi_\alpha = \varphi(\mathbf{R}_\alpha). \tag{16}$$

The physical explanation, why the four phases φ_α should be tracked in the variational solution, is given at the end of Appendix A.

Substituting transformation (8) and (9) into the Hamiltonian (7), and then averaging the result with respect to *B*-operators, I obtain

$$\mathcal{H}_a = 4\varepsilon_b N[s^2 n_B + w^2(1-n_B)] + \varepsilon_a \sum_i a_i^+ a_i + gsw(1-2n_B)\sum_\alpha \left[e^{-i\varphi_\alpha} \sum_i^{\eta_i=1} a_i a_{j(i,\mathbf{R}_\alpha)} + \text{h.c.} \right], \tag{17}$$

where

$$n_B = \frac{1}{\exp\left(\frac{\varepsilon_B}{T}\right)+1}. \tag{18}$$

Here, n_B and ε_B are, respectively, the occupation number and the energy of a *B*-state; and T is the temperature measured in energy units. Index $j(i,\mathbf{R}_\alpha)$ in Eq. (17) labels the nearest neighbor of ith supercell such that $\mathbf{r}_j - \mathbf{r}_i = \mathbf{R}_\alpha$.

At this point, it is convenient to replace supercell indices i and j in Eq. (17) by the set of the radius-vectors and also to separate explicitly the summations over even and odd supercells. This gives

$$\mathcal{H}_a = 4\varepsilon_b N[s^2 n_B + w^2(1-n_B)] + \varepsilon_a \sum_{\mathbf{r}_e} a^+(\mathbf{r}_e)a(\mathbf{r}_e) + \varepsilon_a \sum_{\mathbf{r}_o} a^+(\mathbf{r}_o)a(\mathbf{r}_o) + gsw(1-2n_B) \times \sum_\alpha \left[e^{-i\varphi_\alpha} \sum_{\mathbf{r}_e} a(\mathbf{r}_e)a(\mathbf{r}_e+\mathbf{R}_\alpha) + \text{h.c.} \right], \tag{19}$$

where even supercells are characterized by the discrete set of radius-vectors $\{\mathbf{r}_e\}$ and odd supercells by the complementary discrete set $\{\mathbf{r}_o\}$. Note: any vector of the form $\mathbf{r}_e + \mathbf{R}_\alpha$ belongs to the "odd" subset.

Now I introduce the Fourier transform *separately* for even and odd supercells

$$a_e(\mathbf{k}) = \sqrt{\frac{2}{N}} \sum_{\mathbf{r}_e} a(\mathbf{r}_e) e^{-i\mathbf{k}\mathbf{r}_e}, \tag{20}$$

$$a_o(\mathbf{k}) = \sqrt{\frac{2}{N}} \sum_{\mathbf{r}_o} a(\mathbf{r}_o) e^{-i\mathbf{k}\mathbf{r}_o}. \tag{21}$$

The two Fourier transforms, although involving different parts of real space, still performed with the same set of k-vectors, because the even and the odd subsets have the same periodicity. The projections k_x and k_y of the k-vectors change in discrete steps $2\pi/L_x$ and $2\pi/L_y$, respectively. They fall in the interval $-\pi/d \leqslant k_x, k_y \leqslant \pi/d$, where d is the period of the sublattice of even (or odd) supercells equal to $\ell\sqrt{2}$. The total number of k-vectors is

$$N_k = L_x L_y/(d^2) = N/2. \tag{22}$$

After transformation (20) and (21), the Hamiltonian (19) can be written as

$$\mathcal{H}_a = 4\varepsilon_b N[s^2 n_B + w^2(1-n_B)] + \varepsilon_a \sum_{\mathbf{k}} a_e^+(\mathbf{k})a_e(\mathbf{k}) + \varepsilon_a \sum_{\mathbf{k}} a_o^+(\mathbf{k})a_o(\mathbf{k}) + gsw(1-2n_B) \times \sum_{\mathbf{k}} [a_e(\mathbf{k})a_o(-\mathbf{k})V(\mathbf{k}) + \text{h.c.}], \tag{23}$$

where

$$V(\mathbf{k}) \equiv \sum_\alpha e^{-i\varphi_\alpha - i\mathbf{k}\mathbf{R}_\alpha} = 2\exp\left[-i\frac{\varphi_1+\varphi_3}{2}\right]\cos\left[\mathbf{k}\mathbf{R}_1 + \frac{\varphi_1-\varphi_3}{2}\right] + 2\exp\left[-i\frac{\varphi_2+\varphi_4}{2}\right]\cos\left[\mathbf{k}\mathbf{R}_2 + \frac{\varphi_2-\varphi_4}{2}\right]. \tag{24}$$

Given the form of the interaction term in the Hamiltonian (23), the choice of canonical transformation for *a*-states is clear

$$a_e(\mathbf{k}) = u(\mathbf{k})A_e(\mathbf{k}) + v(\mathbf{k})e^{i\phi_a(\mathbf{k})}A_o^+(-\mathbf{k}), \tag{25}$$

$$a_o(-\mathbf{k}) = u(\mathbf{k})A_o(-\mathbf{k}) - v(\mathbf{k})e^{i\phi_a(\mathbf{k})}A_e^+(\mathbf{k}), \tag{26}$$

where $A_e(\mathbf{k})$ and $A_o(\mathbf{k})$ are annihilation operators of the new Bogoliubov quasiparticles; $\phi_a(\mathbf{k})$ is the phase of this transformation; and $u(\mathbf{k})$ and $v(\mathbf{k})$ are the real numbers obeying the following normalization condition:

$$u^2(\mathbf{k}) + v^2(\mathbf{k}) = 1. \tag{27}$$

An important conceptual detail to be noted here is that transformation (25) and (26) will eventually lead a coherent one-particle dispersion of *A*-quasiparticles in k-space. This kind of k-space coherence emerges only in the SC phase and appears to be "protected" by the Fermi statistics (see the end of Appendix A).

Substitution of transformation (25) and (26) into the Hamiltonian (19) results in the following expression for the energy of the system:

$$E = 4\varepsilon_b N[s^2 n_B + w^2(1-n_B)] + 2\varepsilon_a \sum_{\mathbf{k}} \{u^2(\mathbf{k})n_A(\mathbf{k}) + v^2(\mathbf{k})[1-n_A(\mathbf{k})]\} + 2gsw(1-2n_B) \times \sum_{\mathbf{k}} u(\mathbf{k})v(\mathbf{k})(2n_A(\mathbf{k})-1)|V(\mathbf{k})|\cos[\phi_V(\mathbf{k}) + \phi_a(\mathbf{k})], \tag{28}$$

where $|V(\mathbf{k})|$ and $\phi_V(\mathbf{k})$ are the absolute value and the phase of the complex-valued function (24), and

$$n_A(\mathbf{k}) = \frac{1}{\exp\left(\frac{\varepsilon_A(\mathbf{k})}{T}\right)+1}. \tag{29}$$

Here $n_A(\mathbf{k})$ and $\varepsilon_A(\mathbf{k})$ are, respectively, the occupation number and the energy of a Bogoliubov quasiparticle created by operator $A_e^+(\mathbf{k})$ or $A_o^+(\mathbf{k})$.

It is immediately obvious that the minimization of the above expression requires the last term to have maximally negative value. All the sign conventions used below will be such that $gsw(1-2n_B)u(\mathbf{k})v(\mathbf{k})(2n_A(\mathbf{k})-1)<0$. Therefore, the maximally negative value will be reached, when

$$\cos[\phi_V(\mathbf{k})+\phi_a(\mathbf{k})]=1, \tag{30}$$

which means that (up to an integer number of 2π's)

$$\phi_a(\mathbf{k})=-\phi_V(\mathbf{k}). \tag{31}$$

For the reasons discussed in subsection VI B, the rest of the calculations will be mostly limited to Cases IA, IB, IIA and IIB. Formulas for the critical case will be summarized in subsection VI G. For the general case, only the condensation energy will be obtained (in subsection VI D).

Case IA: $\varepsilon_b=0$, $\varepsilon_a\geqslant 0$.

A natural sign convention in this case is: $\varepsilon_A(\mathbf{k})>0$ and $\varepsilon_B<0$, i.e., at $T=0$, $n_A(\mathbf{k})=0$ and $n_B=1$. Given the above convention, the minimization of energy (28) gives

$$u(\mathbf{k})=\sqrt{\frac{1}{2}+\frac{1}{2}\sqrt{\frac{1}{1+\dfrac{\mathcal{T}^2(\mathbf{k})}{\mathcal{Q}^2(\mathbf{k})}}}}, \tag{32}$$

$$v(\mathbf{k})=\sqrt{\frac{1}{2}-\frac{1}{2}\sqrt{\frac{1}{1+\dfrac{\mathcal{T}^2(\mathbf{k})}{\mathcal{Q}^2(\mathbf{k})}}}}, \tag{33}$$

$$s=\frac{1}{\sqrt{2}}, \tag{34}$$

$$w=-\frac{1}{\sqrt{2}}, \tag{35}$$

where

$$\mathcal{Q}(\mathbf{k})=2\varepsilon_a(2n_A(\mathbf{k})-1), \tag{36}$$

$$\mathcal{T}(\mathbf{k})=g(1-2n_B)(2n_A(\mathbf{k})-1)|V(\mathbf{k})|. \tag{37}$$

By varying E with respect to $n_A(\mathbf{k})$ and n_B, one can now obtain the quasiparticle energies

$$\varepsilon_A(\mathbf{k})=\sqrt{\varepsilon_a^2+\frac{1}{4}g^2(2n_B-1)^2|V(\mathbf{k})|^2}, \tag{38}$$

$$\varepsilon_B=-\frac{g^2(2n_B-1)}{8N}\sum_{\mathbf{k}}\frac{(1-2n_A(\mathbf{k}))|V(\mathbf{k})|^2}{\varepsilon_A(\mathbf{k})} \tag{39}$$

and then express the total energy of the system as

$$E=-\sum_{\mathbf{k}}[(1-2n_A(\mathbf{k}))\varepsilon_A(\mathbf{k})-\varepsilon_a]. \tag{40}$$

Here and everywhere, the summation over $\mathbf{k}$ can be replaced by integration according to the following rule:

$$\frac{1}{N}\sum_{\mathbf{k}}\rightarrow\frac{d^2}{8\pi^2}\int_{-\frac{\pi}{d}}^{\frac{\pi}{d}}dk_x\int_{-\frac{\pi}{d}}^{\frac{\pi}{d}}dk_y. \tag{41}$$

Energy (40) is the function of $|V(\mathbf{k})|$ (via $\varepsilon_A(\mathbf{k})$ and $n_A(\mathbf{k})\equiv n_A[\varepsilon_A(\mathbf{k})]$). In turn, $|V(\mathbf{k})|$ is the function of four phases (16) [via Eq. (24)]. Therefore, energy (40) should be further minimized with respect to the values of those phases. As shown in Appendix B, such a minimization imposes only one constraint

$$\frac{\varphi_2+\varphi_4-\varphi_1-\varphi_3}{2}=\frac{\pi}{2}+\pi n, \tag{42}$$

where n is an integer number. Among three other independent combinations of phases φ_1, φ_2, φ_3 and φ_4, one should remain free as a consequence of the global gauge invariance, while two other combinations should, in principle, be fixed, but not in the framework of the present model.

The main thermodynamic and transport properties of the model are independent of the choice of phases φ_1, φ_2, φ_3 and φ_4 as long as this choice is consistent with Eq. (42). This situation is somewhat similar to that of superfluid ^{3}He, where the interaction causing the superfluid transition does not fix the values of all variables characterizing the order parameter.[49] In ^{3}He, the remaining freedom is eliminated by magnetic dipolar interaction between nuclei, and by other small interactions. In the present case, the same role can be played, e.g., by pair hopping between a-states or b-states belonging to different supercells. In this work, the issue of the "phase freedom" is not resolved. It is, however, possible to speculate that the additional terms will lead to sufficiently symmetric selection of phases, such that

$$V(\mathbf{k})=2\{\cos[\mathbf{kR}_1]-i\cos[\mathbf{kR}_2]\}, \tag{43}$$

or

$$V(\mathbf{k})=2\{\sin[\mathbf{kR}_1]-i\sin[\mathbf{kR}_2]\}, \tag{44}$$

or

$$V(\mathbf{k})=2\{\cos[\mathbf{kR}_1]-i\sin[\mathbf{kR}_2]\}. \tag{45}$$

The first choice corresponds to $\varphi_1=\varphi_3=0$, $\varphi_2=\varphi_4=\pi/2$; the second one to $\varphi_1=-\pi/2$, $\varphi_2=0$, $\varphi_3=\pi/2$, and $\varphi_4=\pi$; and the third one to $\varphi_1=0$, $\varphi_2=0$, $\varphi_3=0$, and $\varphi_4=\pi$; The resulting patterns of phases are shown in Fig. 6.

Having specified the parameters of transformations (8), (9), (25), and (26), one can calculate the temperature dependence of various thermodynamic quantities. This requires a numerical solution of the system of equations (18), (29), (38), and (39), which is not done in the present work. Without the full numerical solution only the zero-temperature characteristics and the SC transition temperature T_c can be evaluated. The evaluation of T_c is based on a manipulation described in Appendix C, which gives the following simple equation:

$$T_c=\frac{g^2\left[\exp\left(\dfrac{\varepsilon_a}{T_c}\right)-1\right]}{8\varepsilon_a\left[\exp\left(\dfrac{\varepsilon_a}{T_c}\right)+1\right]}. \tag{46}$$

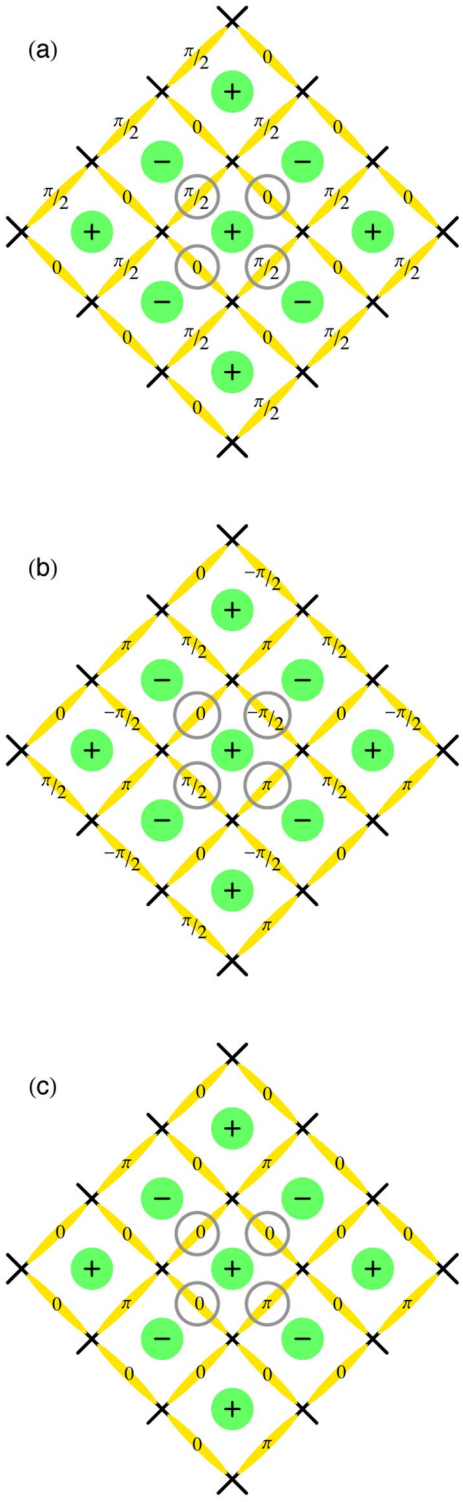

FIG. 6. (Color online) Three examples of particularly symmetric patterns of phases φ_{ij} consistent with the variational SC solution. The values of the phases are indicated on the top of the corresponding stripe elements. Each pattern is obtained by the periodic translation of four circled phases denoted in the text as φ_α. These phases are constrained by Eq. (42). The expressions for $V(\mathbf{k})$ corresponding to the phase patterns (a), (b) and (c) are given, in respective order, by Eqs. (43)–(45).

When $g \leqslant \varepsilon_a$, the approximate solution of Eq. (46) is

$$T_c \cong \frac{g^2}{8\varepsilon_a}. \tag{47}$$

Another simple limit is $\varepsilon_a = 0$, in which case Eq. (46) yields

$$T_c = \frac{g}{4}. \tag{48}$$

In general, however, Eq. (46) has to be solved numerically.

Since the operators of both real holes and real electrons do not commute with A- and B-operators defined by Eqs. (A1)–(A3), the tunneling studies of both A- and B-quasiparticles (via a contact with normal metal) should show the density of states on the both sides of the chemical potential, i.e., at $\varepsilon = \pm\varepsilon_A$ and $\varepsilon = \pm\varepsilon_B$. Moreover, as long as $\varepsilon_b = 0$, tunneling into B-states should result in the density of states symmetric with respect to the chemical potential. As far as A-states are concerned, then tunneling into them should show asymmetric density of states. This asymmetry is characterized by the ratio

$$\frac{D[\varepsilon_A(\mathbf{k})]}{D[-\varepsilon_A(\mathbf{k})]} = \frac{u^2(\mathbf{k})}{v^2(\mathbf{k})} = \frac{\varepsilon_A(\mathbf{k}) + \varepsilon_a}{\varepsilon_A(\mathbf{k}) - \varepsilon_a}. \tag{49}$$

The zero-temperature tunneling spectra of A- and B-quasiparticles are shown in Fig. 7(a). The spectrum of B-quasiparticles consists of two delta-peaks located at $\pm\varepsilon_B$. A-quasiparticles have a continuous spectrum, which is fully gapped with minimal energy ε_a. It was obtained by first calculating the density of states following from Eq. (38) as a function of positive energies ε_A and then dividing the weight between positive and negative tunneling energies according to formula (49).

In addition to the gap and the asymmetry, two other important features of the spectrum of A-quasiparticles are: the Van Hove singularity and the sharp termination point at a higher energy. These two features correspond, respectively, to the saddle points and to the maxima of $|V(\mathbf{k})|$. Function $|V(\mathbf{k})|$ obtained from Eq. (43) is shown in Fig. 8. It has four saddle points at $\mathbf{k}_S = \pi/2d(\pm 1, \pm 1)$. With another choice of phases consistent with Eq. (42), the k-space position of the saddle points may change but not the value of $|V(\mathbf{k}_S)| = 2$. Therefore, according to Eq. (38), the density of A-states exhibits a Van Hove singularity at

$$\varepsilon_{A0} = \sqrt{\varepsilon_a^2 + g^2(2n_B - 1)^2}. \tag{50}$$

The maximum energy of A-states, which corresponds to the tunneling spectrum termination point, can be found by substituting the maximum value of $|V(\mathbf{k})|$ equal to $2\sqrt{2}$ into Eq. (38), which gives

$$\varepsilon_{A1} = \sqrt{\varepsilon_a^2 + 2g^2(2n_B - 1)^2}. \tag{51}$$

It should be noted here that the appearance of the tunneling spectrum of A-states shown in Fig. 7(a) is quite similar to that of the fermion spectrum obtained by Altman and Auerbach from the plaquette boson-fermion model.[28]

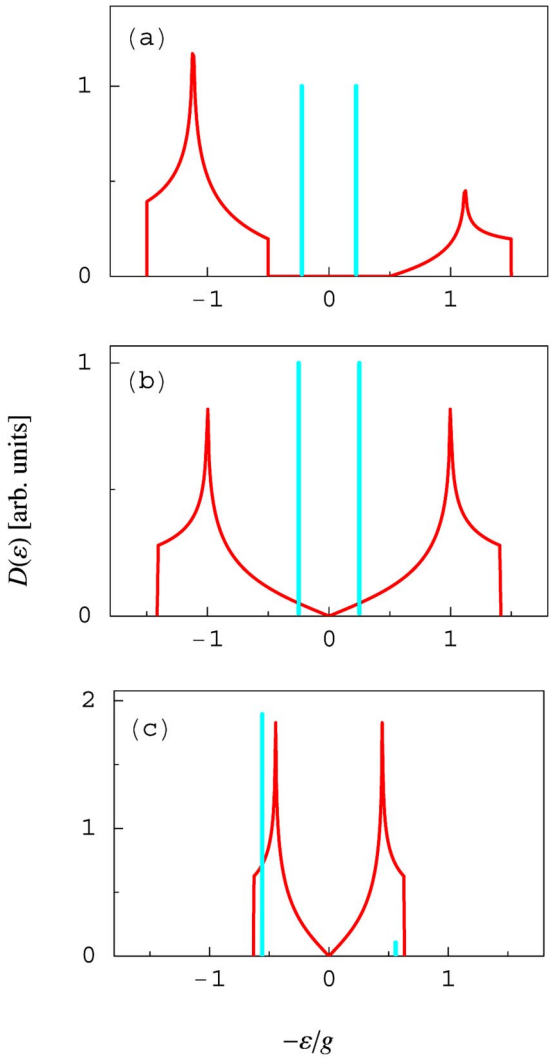

FIG. 7. (Color online) Examples of the tunneling density of states at $T=0$: (a) Case IA ($\varepsilon_a=0.5g, \varepsilon_b=0$); (b) critical case ($\varepsilon_a=0, \varepsilon_b=0$); (c) Case IIA ($\varepsilon_a=0, \varepsilon_b=0.5g$). In each case, the spectra contain two vertical delta-peaks representing *B*-states and located at $\pm\varepsilon_B$ given by (a) Eq. (38); (b,c) Eq. (59). The continuous part in each spectrum represents *A*-states. It is calculated from: (a) Eq. (38); (b,c) Eq. (59). In all three cases, the spectra of *A*-states have Van-Hove singularities located at $\pm\varepsilon_{A0}$ and the termination points located at $\pm\varepsilon_{A1}$. The spectrum of *A*-states in figure (a) also has a gap between ε_a and $-\varepsilon_a$. The asymmetry of the spectra is obtained from: (a) Eq. (49); (c) Eq. (64). Note: the positive direction of the horizontal axis corresponds to negative hole energies. (This reflects a convention of tunneling spectroscopy.)

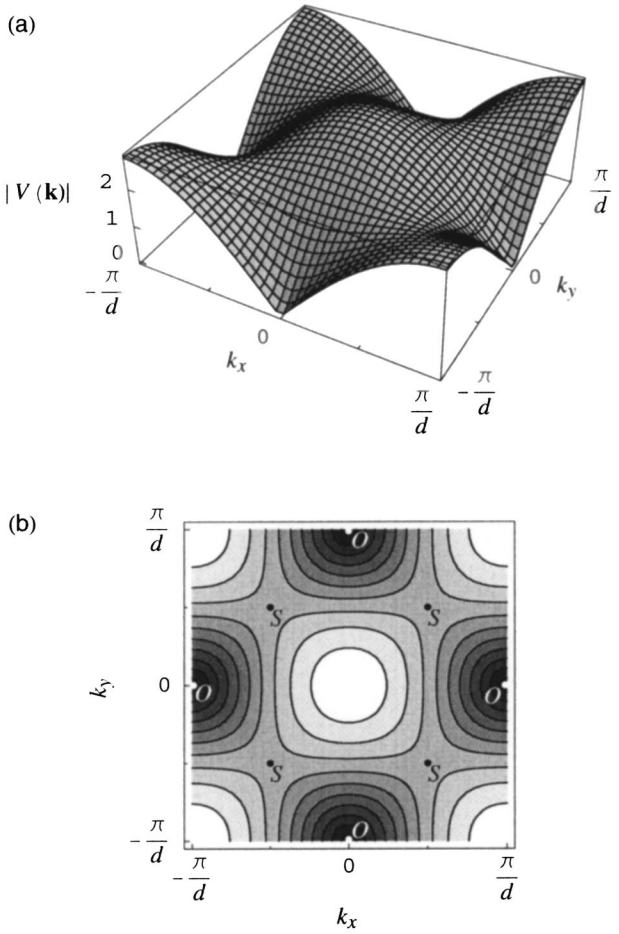

FIG. 8. (a) Three-dimensional plot and (b) contour plot of $|V(\mathbf{k})|$ corresponding to Eq. (43). Each plot shows the first Brillouin zone of the stripe superstructure. In the contour plot, the saddle points are indicated with "*S*," and zeros with "*O*."

Case IB: $\varepsilon_b=0$, $\varepsilon_a\leqslant 0$.

In this case, if one keeps the same sign convention as in Case IA, then $u(\mathbf{k})$ and $v(\mathbf{k})$ given by Eqs. (32) and (33) should switch values. All formulas for the quasiparticle energies and the tunneling spectrum asymmetry obtained for Case IA apply without modification to the present case. Equation (46) for the critical temperature also applies but with the trivial substitution of $|\varepsilon_a|$ instead of ε_a.

The only observable difference between Cases IA and IB is the opposite asymmetry with respect to the chemical potential: in Case IA, the density of *A*-states is greater on the hole side, while, in Case IB, on the electron side.

Case IIA: $\varepsilon_a=0$, $\varepsilon_b\geqslant 0$.

The sign convention in this case is chosen to be opposite to that of Case IA, namely: $\varepsilon_A(\mathbf{k})<0$ and $\varepsilon_B>0$, i.e., at $T=0$, $n_A(\mathbf{k})=1$ and $n_B=0$.

In this case

$$u(\mathbf{k})=\frac{1}{\sqrt{2}}, \tag{52}$$

$$v(\mathbf{k})=\frac{1}{\sqrt{2}}, \tag{53}$$

$$s=\sqrt{\frac{1}{2}+\frac{1}{2}\sqrt{\frac{1}{1+\frac{\mathcal{T}^2}{\mathcal{Q}^2}}}}, \tag{54}$$

$$w = -\sqrt{\frac{1}{2} - \frac{1}{2}\sqrt{\frac{1}{1+\frac{\mathcal{T}^2}{\mathcal{Q}^2}}}}, \tag{55}$$

where

$$\mathcal{Q} = 4N\varepsilon_b(2n_B - 1), \tag{56}$$

$$\mathcal{T} = g(1-2n_B)C_a N, \tag{57}$$

$$C_a = \frac{1}{N}\sum_{\mathbf{k}} (2n_A(\mathbf{k}) - 1)|V(\mathbf{k})|. \tag{58}$$

One can then obtain the quasiparticle energies

$$\varepsilon_A(\mathbf{k}) = -\frac{g^2|V(\mathbf{k})|C_a(1-2n_B)}{8\varepsilon_B}, \tag{59}$$

$$\varepsilon_B = \sqrt{\varepsilon_b^2 + \frac{1}{16}g^2C_a^2} \tag{60}$$

and the total energy

$$E = -2N[(1-2n_B)\varepsilon_B - \varepsilon_b]. \tag{61}$$

The choice of phases (16) is still constrained by condition (42) (see Appendix B). Given this constraint, the zero temperature value of C_a (obtained numerically) is

$$C_{a0} \equiv \frac{1}{N}\sum_{\mathbf{k}} |V(\mathbf{k})| = 0.958\ldots. \tag{62}$$

A manipulation analogous to the one described in Appendix C gives the following equation for the critical temperature:

$$T_c = \frac{g^2\left[\exp\left(\frac{\varepsilon_b}{T_c}\right) - 1\right]}{8\varepsilon_b\left[\exp\left(\frac{\varepsilon_b}{T_c}\right) + 1\right]}. \tag{63}$$

The tunneling density of states corresponding to Eqs. (59) and (60) is shown in Fig. 7(c). Contrary to the result for Case I, the tunneling density of *A*-states in Case II is symmetric, while the density of *B*-states is asymmetric. This asymmetry is characterized by the ratio

$$\frac{D(\varepsilon_B)}{D(-\varepsilon_B)} = \frac{s^2}{w^2} = \frac{\varepsilon_B + \varepsilon_b}{\varepsilon_B - \varepsilon_b}. \tag{64}$$

An important feature of Case II, which is absent in Case I, is that the energy spectrum of *A*-quasiparticles is gapless with the linear density of states around the chemical potential. Indeed, $\varepsilon_A(\mathbf{k})$ given by Eq. (59) touches zero in an isolated set of nonanalytic points corresponding to $|V(\mathbf{k})|=0$. For the specific choice of $V(\mathbf{k})$ given by Eq. (43), the zeros of $|V(\mathbf{k})|$ are shown in Fig. 8. They are located at $\mathbf{k}_0 = \frac{\pi}{d}(\pm 1, 0)$ and $\mathbf{k}_0 = \frac{\pi}{d}(0, \pm 1)$. This feature is a direct consequence of the phase relation (42). A deviation from that relation would produce a line of zeros, which implies a nonzero density of states at $\varepsilon_A = 0$.

The density of *A*-states in Case IIA has Van Hove singularity and the termination point located, respectively, at

$$\varepsilon_{A0} = -\frac{g^2C_a(1-2n_B)}{4\varepsilon_B} \tag{65}$$

and

$$\varepsilon_{A1} = \sqrt{2}\varepsilon_{A0}. \tag{66}$$

Case IIB: $\varepsilon_a = 0$, $\varepsilon_b \leqslant 0$.

All formulas for the quasiparticle energies and the tunneling spectrum asymmetry obtained for Case IIA apply without modification to Case IIB. Equation (63) for the critical temperature only requires the substitution of $|\varepsilon_b|$ instead of ε_b. The only difference between Cases IIA and IIB is the opposite asymmetries in the tunneling spectra of *B*-quasiparticles. In Case IIA, the hole side of the *B*-quasiparticle spectrum has more weight, while in Case IIB, the larger weight is on the electron side.

D. Chemical potential as a variational parameter

In this subsection, I argue that the situations corresponding to $\mu = \varepsilon_b$ (Case I) or $\mu = \varepsilon_a$ (Case II) should be considered as likely scenarios describing realistic stripe systems.

The constraint on the total number of particles, which is usually used to fix μ, cannot be straightforwardly applied to the present model for the following reasons: (i) The model quantum states form a subset of all quantum states of a real "striped" system, and, therefore, the actual total number of particles cannot be reliably counted. (ii) The system can always readjust the periodicity of the stripe superstructure, which would change the ratio between the number of model states and the number of holes doped into CuO_2 planes. (iii) The chemical potential can change within the model pseudogap without affecting the total number of particles occupying model states (at $T=0$).

It is, therefore, reasonable to treat the chemical potential as a variational parameter, which is fixed by the minimization of the total energy of the real system considered as the sum of the contribution from the model states and the contribution from environment (unspecified here).

The model contribution to the total energy as a function of the chemical potential can be obtained by solving the model in the general case: $\varepsilon_a \neq 0$, $\varepsilon_b \neq 0$. The description of general case is as straightforward as that of Cases I and II. However, the minimization routine produces an integral equation, which couples the values of $u(\mathbf{k})$, $v(\mathbf{k})$, s and w, and which has to be solved numerically.

Figure 9 shows three representative curves for the evolution of the SC ground state energy as a function of the chemical potential. Each curve was obtained numerically for the fixed values of ε_a, ε_b and g indicated in the caption. In order to allow for the variation of μ, the reference point for one-particle energies was shifted (in this part only) from $\mu=0$ to some arbitrary value $\varepsilon_b=0$. The SC ground state energy was measured from the energy of the normal state. The absolute value of thus defined quantity is conventionally called condensation energy.

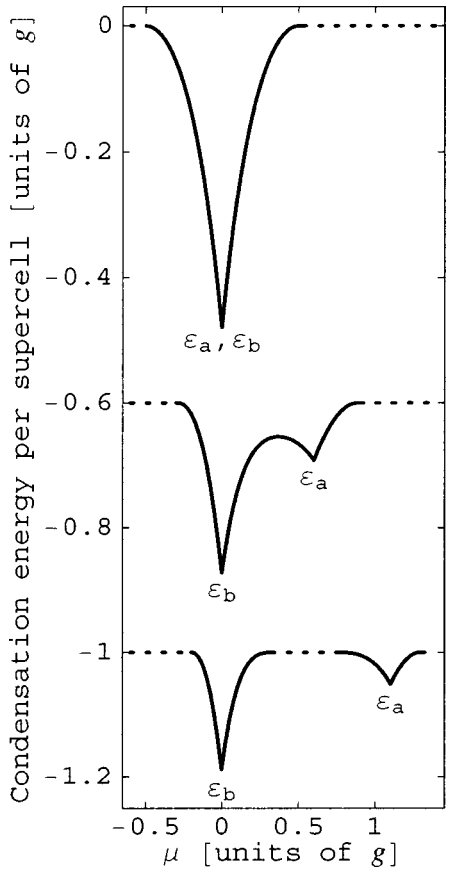

FIG. 9. Condensation energy (with the negative sign) as a function of the chemical potential μ. Each of the three curves was calculated on the basis of Hamiltonian (7) by fixing ε_a, ε_b and g and then varying μ. In the calculations, g and ε_b were equal, respectively, to 1 and 0 in all three cases, while ε_a admitted the following values (top to bottom): 0, 0.6 and 1.1. The solid/dashed lines indicate the SC/non-SC ground state. The deeper minima of the lower two curves correspond to Case I, and the shallower ones to Case II. The single minimum of the top curve corresponds to the critical case. The vertical coordinates of the middle and the bottom curves are shifted by −0.6 and −1, respectively.

In a generic situation (two lower curves in Fig. 9), the ground state energy has two minima: the deeper one—corresponding to Case I, and the shallower one—corresponding to Case II. For a fixed value of g, the SC transition is possible only, when the value of μ lies close enough to either ε_a or ε_b. Dependently on the ratio $|\varepsilon_a - \varepsilon_b|/g$, the values of μ compatible with superconductivity fill either one finite interval including both ε_a and ε_b or two disconnected finite intervals around ε_a and ε_b. The top curve in Fig. 9 illustrates a nongeneric situation, when the two minima coincide. The resulting single minimum then corresponds to the critical case.

The main purpose of Fig. 9 is to illustrate, that, not only do Cases I and II correspond to local minima in the μ dependence of the ground state energy, but also that these minima have the form of cusps. This implies that, if the environment contribution to the total energy of the model-plus-environment system is a smooth function of μ, then the total energy should have the cusp minima due to the model contribution at exactly the same values of μ as those obtained without environment. If only the model contribution were taken into account, then it would follow from Fig. 9 that the minimum corresponding to Case I is the global one. However, the environment contribution can change the relative values of energies, corresponding to the two minima and thus shift the global minimum to that of Case II.

In principle, it is also possible that environment introduces an extra energy minimum in addition to the two cusps described above, and, moreover, that additional minimum is the global one.

The resulting possibilities can be summarized as follows: Cases I and II of the present model describe two different SC states corresponding to two different positions of the chemical potential. In the "best case" scenario (which I also consider more likely), one of these two states corresponds to the global energy minimum of the real system, while the other one represents a metastable state. In the "worst case" scenario, both SC states are metastable, but the true SC state may still be describable by the present model with $\varepsilon_a \neq 0$ and $\varepsilon_b \neq 0$.

It is further possible that the position of the chemical potential near the sample surface is different from that in the bulk. Therefore, the SC state, which is metastable in the bulk, may become stable near the surface and *vice versa*. In principle, it is also possible that the system phase separates and forms domains describable either by Case I or by Case II.

In Sec. VIII E, I will try to discriminate between the SC states corresponding to Cases I and II by making a comparison between the model predictions and the experiments.

E. Anomalous correlation functions

Bogoliubov transformations (8), (9), (25), and (26) imply that, below T_c, the following anomalous correlation functions have nonzero values:

$$\Psi_a(\mathbf{k}) = \langle a_e(\mathbf{k}) a_o(-\mathbf{k}) \rangle = u(\mathbf{k}) v(\mathbf{k}) e^{\phi_a(\mathbf{k})} [2n_A(\mathbf{k}) - 1], \tag{67}$$

$$\Psi_b(\mathbf{r}_{ij}, \mathbf{r}_{pn}) \equiv \langle b_{ij,-} b_{pn,+} \rangle = sw e^{i\varphi_{ij}} (1 - 2n_B) \delta(\mathbf{r}_{ij} - \mathbf{r}_{pn}), \tag{68}$$

where $\mathbf{r}_{ij}$ represents the positions of the centers of stripe elements, and $\delta(\ldots)$ is defined as Kronneker delta on the discrete superlattice, i.e., it is equal to 1, when its argument is zero, and 0 otherwise. The two correlation functions (67) and (68) are the two components of the SC order parameter corresponding to *a*- and *b*-states, respectively.

In the real space, the first component can be defined as

$$\Psi_a(\mathbf{r}_i, \mathbf{r}_j) \equiv \langle a(\mathbf{r}_i) a(\mathbf{r}_j) \rangle. \tag{69}$$

It has nonzero values only when its two arguments correspond to the supercells of different kind (i.e., even and odd). The formal structure of $\Psi_a(\mathbf{r}_i, \mathbf{r}_j)$ can be expressed as follows:

$$\Psi_a(\mathbf{r}_e, \mathbf{r}_o) = \frac{2}{N} \sum_{\mathbf{k}} \Psi_a(\mathbf{k}) e^{i\mathbf{k}(\mathbf{r}_e - \mathbf{r}_o)}, \tag{70}$$

$$\Psi_a(\mathbf{r}_o,\mathbf{r}_e) = -\Psi_a(\mathbf{r}_e,\mathbf{r}_o), \tag{71}$$

$$\Psi_a(\mathbf{r}_e,\mathbf{r}'_e) = \Psi_a(\mathbf{r}_o,\mathbf{r}'_o) = 0, \tag{72}$$

where $\Psi_a(\mathbf{k})$ is given by Eq. (67). Note: Eq. (71) is the consequence of the fermionic anticommutation rule.

The coherence length of the order parameter $\Psi_a(\mathbf{r}_i,\mathbf{r}_j)$ should be inversely proportional to the one characterizing $V(\mathbf{k})$ in k-space. The examination of Eq. (24) reveals that the characteristic scale of $V(\mathbf{k})$ is $\pi/|\mathbf{R}_1| = \pi/\ell$. Therefore, the coherence length associated with $\Psi_a(\mathbf{r}_i,\mathbf{r}_j)$ can be estimated as the supercell size ℓ. It is likely, that on a longer scale $\Psi_a(\mathbf{r}_i,\mathbf{r}_j)$ exhibits an oscillatory power law decay with the period of oscillations being of the order of ℓ.

The coherence length associated with Ψ_b is equal to zero, which means that only b-states belonging to the same stripe element form coherent pairs.

Two useful quantities, which will later be required in the calculation of supercurrent, are

$$\Psi_{a(ij)} \equiv \Psi_a^{\text{n.n.}}(\mathbf{r}_i,\mathbf{r}_j) \equiv \langle a_i a_j\rangle^{\text{n.n.}} \tag{73}$$

and

$$\Psi_{b(ij)} \equiv \Psi_b(\mathbf{r}_{ij},\mathbf{r}_{ij}) \equiv \langle b_{ij,-} b_{ij,+}\rangle, \tag{74}$$

where the superscript "n.n." indicates that indices i and j represent the nearest neighbors.

In Case I, the explicit expression for $\Psi_{b(ij)}$ can be obtained by substituting the values of s and w given by Eqs. (34) and (35) into Eq. (68) for $\mathbf{r}_{ij}=\mathbf{r}_{pn}$, which gives

$$\Psi_{b(ij)} = \frac{1}{2} e^{i\varphi_{ij}}(2n_B - 1). \tag{75}$$

One can then obtain $\Psi_{a(ij)}$ by making use of the fact that

$$\Psi^*_{b(ij)}\Psi_{a(ij)} = \frac{E_{\text{int}}}{4gN}, \tag{76}$$

where E_{int} is the interaction part of the energy (28) (i.e., $E_{\text{int}}=2gsw(1-2n_B)\Sigma_{\mathbf{k}}\ldots$). After E_{int} is evaluated with the help of Eqs. (32)–(35), one can use Eqs. (75) and (76) to obtain

$$\Psi_{a(ij)} = \frac{g(1-2n_B)\,\eta_i e^{i\varphi_{ij}}}{8N}\sum_{\mathbf{k}} \frac{[1-2n_A(\mathbf{k})]|V(\mathbf{k})|^2}{\varepsilon_A(\mathbf{k})}. \tag{77}$$

The role of index η_i in Eq. (77) is to supply factor 1 or −1 dependently on whether the first index of $\Psi_{a(ij)}$ corresponds to an even or an odd supercell.

In Case II, the expressions analogous to Eqs. (77) and (75) are

$$\Psi_{a(ij)} = \frac{1}{4}\eta_i e^{i\varphi_{ij}}, \tag{78}$$

$$\Psi_{b(ij)} = -\frac{gC_a e^{i\varphi_{ij}}(1-2n_B)}{8\varepsilon_B}. \tag{79}$$

The essential elements of the symmetry of the SC order parameter (75) and (77) or, alternatively, Eqs. (78) and (79) are captured in Fig. 6. This symmetry is characterized by the pattern of phases φ_{ij} indicated on the top of each stripe element, and, in addition, by the pattern of index η_i.

The order parameter $\Psi_b(\mathbf{r}_{ij},\mathbf{r}_{pn})$ has no dependence on the relative orientation of $\mathbf{r}_{ij}$ and $\mathbf{r}_{pn}$. Therefore, it can be described as having orientational s-wave symmetry with additional strong phase dependence on the center-of-mass position of the paired holes.

The symmetry of $\Psi_a(\mathbf{r}_i,\mathbf{r}_j)$ is even more different from conventional analogs. It includes the strong dependence on φ_{ij}, which traces the phase dependence of $\Psi_b(\mathbf{r}_{ij},\mathbf{r}_{pn})$, but, in addition, $\Psi_a(\mathbf{r}_i,\mathbf{r}_j)$ also exhibits a sign change under the translation by one period of the stripe superstructure. This sign change reflects the switching between even/odd and odd/even order in Eq. (71).

F. Supercurrent and the penetration depth

The superconducting properties of the present model are unusual, because the superconducting phase stiffness comes solely from the interaction term of the Hamiltonian (7). This term induces the fundamental "internal supercurrent" associated with the transfer of particle density from a-states to b-states and *vice versa*. The translational supercurrent then appears as a gradient of the internal one.

The operator expression for the internal current from ith a-state to the surrounding b-states can be obtained by considering the time derivative of the particle density operator

$$J_{ab(i)} \equiv -\frac{d}{dt}(a_i^+ a_i) = -\frac{i}{\hbar}[\mathcal{H}a_i^+ a_i - a_i^+ a_i \mathcal{H}]$$
$$= -\frac{ig}{\hbar}\sum_{j(i)}(b^+_{ij,+}b^+_{ij,-}a_i a_j - \text{h.c.}). \tag{80}$$

Here and everywhere in this subsection, index i corresponds to an even supercell, and index j to an odd one.

The sum in Eq. (80) has four terms—each corresponding to the transfer of the particle density from the ith AF domain into a nearby stripe element labeled by the pair of indices ij. Therefore, the operator of translational current through the ith supercell (to be denoted as $\mathbf{J}_i^t$) can be obtained by assigning the direction to the flow of particle density associated with each of the above four terms, i.e.

$$\mathbf{J}_i^t = -\frac{ig}{2\hbar}\sum_{j(i)}\hat{\mathbf{n}}_{ij}(b^+_{ij,+}b^+_{ij,-}a_i a_j - \text{h . c . }), \tag{81}$$

where $\hat{\mathbf{n}}_{ij}$ is the unit vector in the direction from the ith to the jth supercell.

The translational current is created when the probability of an a-particle to hop into one of the surrounding stripe elements is greater in one direction than in the opposite one. For this reason, the translational current can only be carried by a-states. The number of b-particles hopping on the both sides of a given stripe element is the same for each quantum transition generated by the Hamiltonian (7).

Now, I show that the phase, which drives the internal *supercurrent*, is

$$\phi_{ab} = -\phi_a(\mathbf{k}) - \phi_V(\mathbf{k}). \tag{82}$$

In equilibrium, according to Eq. (31), $\phi_{ab}=0$. The state with nonzero ϕ_{ab} can be obtained by modifying the Bogoliubov transformation for *b*-states [Eqs. (8) and (9)] as follows:

$$b_{ij+} = sB_{ij+} + we^{i(\varphi_{ij}+\phi_{ab})}B^{+}_{ij-}, \tag{83}$$

$$b_{ij-} = sB_{ij-} - we^{i(\varphi_{ij}+\phi_{ab})}B^{+}_{ij+} \tag{84}$$

while keeping the transformation (25) and (26) for *a*-states unchanged. In this case, the anomalous correlation functions are, for *a*-states belonging to the neighboring supercells

$$\langle a_i a_j \rangle = \Psi_{a(ij)} \tag{85}$$

and, for *b*-states belonging to the same stripe element

$$\langle b_{ij-} b_{ij+} \rangle = \Psi_{b(ij)} e^{i\phi_{ab}}, \tag{86}$$

where $\Psi_{a(ij)}$ and $\Psi_{b(ij)}$ are the *equilibrium* values of the two SC components given, in Case I, by Eqs. (75) and (77), and, in Case II, by Eqs. (78) and (79).

The averaging of operator (80) with the subsequent substitution of Eqs. (85) and (86) gives the internal supercurrent

$$\langle J_{ab(i)} \rangle = -\frac{2g \sin \phi_{ab}}{\hbar} \sum_{j(i)} \Psi^{*}_{b(ij)} \Psi_{a(ij)}. \tag{87}$$

Each term in the above sum is a real number given by Eq. (76). [Spatially homogeneous internal supercurrent (87) can exist, when the particle density oscillates between *a*- and *b*-states.]

The translational supercurrent emerges, when ϕ_{ab} becomes position dependent [to be denoted as $\phi_{ab}(\mathbf{r}_{ij})$]. In this case, the relevant Bogoliubov transformation for *b*-states is

$$b_{ij+} = sB_{ij+} + we^{i[\varphi_{ij}+\phi_{ab}(\mathbf{r}_{ij})]}B^{+}_{ij-}, \tag{88}$$

$$b_{ij-} = sB_{ij-} - we^{i[\varphi_{ij}+\phi_{ab}(\mathbf{r}_{ij})]}B^{+}_{ij+}. \tag{89}$$

The transformation for *a*-states is still given by Eqs. (25) and (26). The averaging of Eq. (81) under the assumption that phases $\phi_{ab}(\mathbf{r}_{ij})$ are small and have weak positional dependence, gives the following expression for the translational supercurrent

$$\langle \mathbf{J}^{t}_{i} \rangle = -\frac{g\ell}{\hbar} \Psi^{*}_{b(ij)} \Psi_{a(ij)} \nabla \phi_{ab}. \tag{90}$$

Note: according to Eq. (76), the value of the product $\Psi^{*}_{b(ij)}\Psi_{a(ij)}$ is independent of the orientation of the stripe element labeled by indices ij.

From Eq. (90), the supercurrent density can be obtained as

$$\mathbf{j} = \frac{e}{\ell z_0} \langle \mathbf{J}^{t}_{i} \rangle = S_\phi \nabla \phi_{ab}, \tag{91}$$

where

$$S_\phi = -\frac{eg}{\hbar z_0} \Psi^{*}_{b(ij)} \Psi_{a(ij)}, \tag{92}$$

z_0 is the transverse distance per one SC plane, and e the charge of electron. As follows from Eq. (91), the unconventional feature of the present model is that the supercurrent is induced not by the phase gradients of Ψ_a and Ψ_b separately, but by the gradient of the phase difference between Ψ_a and Ψ_b. Keeping up with convention in the literature, I will refer to the phase stiffness S_ϕ as "superfluid density," but the intuitive associations with some kind of real density would be misleading in this case.

In Case I, the substitution of Eqs. (75) and (77) into Eq. (92) gives

$$S_\phi = \frac{eg^2(1-2n_B)^2}{16N\hbar z_0} \sum_{\mathbf{k}} \frac{(1-2n_A(\mathbf{k}))|V(\mathbf{k})|^2}{\varepsilon_A(\mathbf{k})} \tag{93}$$

and, in Case II, the analogous Eqs. (78) and (79) lead to

$$S_\phi = \frac{eg^2(1-2n_B)C_a^2}{32\hbar z_0 \varepsilon_B}. \tag{94}$$

Now I calculate the in-plane penetration depth λ of magnetic field directed perpendicularly to the SC planes.

The natural expectation is that the gauge-invariant generalization of Eq. (91) accounting for the presence of the vector potential of electromagnetic field $\mathbf{A}$ has form

$$\mathbf{j} = S_\phi \left(\nabla \phi_{ab} - \frac{2e}{\hbar c} \mathbf{A} \right), \tag{95}$$

where c is the speed of light. In the present work, I do not derive Eq. (95) but take it as an additional postulate.

The equivalent of the London limit in the present model is $\lambda \gg \ell$. In this limit, the standard result[50] for the penetration depth, which follows from Eq. (95), is

$$\lambda = \sqrt{\frac{\hbar c^2}{8\pi e S_\phi}}. \tag{96}$$

For the numbers relevant to high-T_c cuprates, the value of S_ϕ is very small, i.e., λ is large, and, therefore, the London limit is well fulfilled (see the estimate in the end of subsection VI G).

The vector potential entering Eq. (95) should be interpreted as describing magnetic field averaged over a large number of supercells. It is, therefore, possible, that, on the scale of ℓ, the true magnetic field fluctuates around the exponentially decaying penetration profile characterized by λ.

The relationship between T_c and the zero-temperature superfluid density (represented as $1/\lambda^2$) is plotted in Fig. 10. The points in this plot were obtained by fixing the value of the interaction constant g and then varying ε_a (in Case I) or ε_b (in Case II) from zero to very large values. The T_c-coordinate of each plot point was obtained by taking a pair of values (ε_a, g) or (ε_b, g) and then solving numerically Eqs. (46) and (63) for Cases I and II, respectively. The $1/\lambda^2$ coordinate was obtained for the same values of (ε_a, g) or (ε_b, g) by calculating S_ϕ according to Eqs. (93) or (94). The theoretical plot of Fig. 10 is compared with experiments in Sec. VIII D.

G. Critical case: $\varepsilon_a = \varepsilon_b = 0$

In the critical case, all the formulas obtained earlier have very simple form. In particular, the SC transition temperature

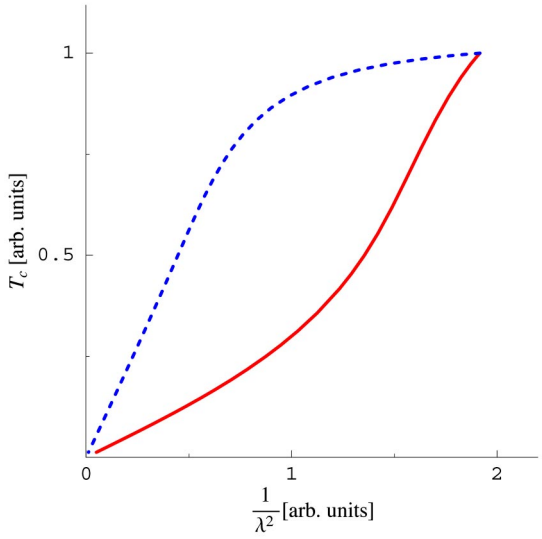

FIG. 10. (Color online) Critical temperature vs superfluid density (represented as $1/\lambda^2$) at $T=0$: solid line—Case I; dashed line—Case II. The plot points are calculated as described in the text.

is given by Eq. (48), which is rewritten here as

$$g = 4T_c. \tag{97}$$

Substituting Eq. (97) and $\varepsilon_a = 0$ into Eqs. (38)–(40), (50), and (93) and using Eq. (62) when necessary, the zero-temperature values of several key quantities can be expressed as follows:

$$\varepsilon_{A0} = 4T_c, \tag{98}$$

$$\varepsilon_B = C_{a0}T_c, \tag{99}$$

$$E_{\mathrm{GS}} = -2C_{a0}T_cN \tag{100}$$

and, finally

$$\lambda = \frac{\hbar c}{2e}\sqrt{\frac{z_0}{\pi C_{a0}T_c}}. \tag{101}$$

The tunneling spectrum for the critical case is shown in Fig. 7(b).

I now assume that one model layer represents one copper-oxide layer of a real compound, which allows me to express the condensation energy per one in-plane copper atom as

$$U_0 = \frac{|E_{\mathrm{GS}}|a_0^2}{N\ell^2} = \frac{2C_{a0}T_ca_0^2}{\ell^2}. \tag{102}$$

Substituting $T_c = 90$ K, $\ell = 4a_0\sqrt{2} \approx 23$ Å and $z_0 = 6$ Å into Eqs. (98), (99), (101), and (102) and recalling that $C_{a0} = 0.958\ldots$, I obtain: $\varepsilon_{A0} = 31$ meV, $\varepsilon_B = 7.4$ meV, $U_0 = 5.4$ K and $\lambda = 417$ nm.

VII. DISCUSSION

A. Realistic features of the model

In this subsection I list the features, which I expect will survive the adaptation of the above model to the properties of real materials, if the 2D diagonal stripe hypothesis turns out to be correct.

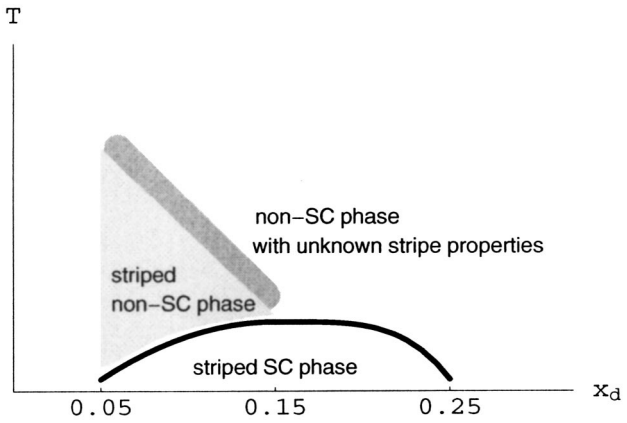

FIG. 11. Cuprate phase diagram proposed in the text.

The basic underlying feature of this model—the potential background, which localizes both *a*- and *b*-states,—should survive the generalizations. In particular, the actual shape of the AF domains can be quite distorted and thus noticeably different from the perfect diamond shape drawn in Fig. 1. It is only important that the stripes divide the plane into finite AF domains with the alternating sign of the AF order parameter. In the model, the disorder in the shape of AF domains can be accommodated through the disorder in the values of ε_a, ε_b and g.

Other supposedly realistic features include the coherence length of the order of ℓ and the decrease of the critical temperature with the increase of $|\varepsilon_a - \varepsilon_b|$, which is associated with the pseudogap.

Finally, the very unconventional translational symmetry of the SC order parameter described in Sec. VI E should also survive generalizations.

B. Phase diagram

In this part, I give the description of the phase diagram of high-T_c cuprates, which is based, in part, on the SC model of Sec. VI, and, in another part, on a few facts borrowed from the next section, where the model predictions are compared with experiments. The phase diagram itself is shown in Fig. 11.

I start at doping concentration $x_d \approx 0.06$. From the viewpoint of the hypothesis adopted in this work, this is the lowest concentration at which the 2D stripe pattern stabilizes by virtue of some unknown energy balance. At this concentration, according to the description given in Secs. II, V, and VI: (i) the length of the stripe supercell can be estimated as $\ell = 1/(2x_d) \approx 8$ lattice sites; (ii) $\varepsilon_a > \varepsilon_b$; (iii) the value of the pseudogap $\varepsilon_a - \varepsilon_b$ is maximal; and (iv) the superconducting transition temperature is minimal.

At higher doping concentrations, the size of the AF domains decreases, eventually saturating at $\ell \approx 4a_0\sqrt{2}$. Simultaneously, the pseudogap $\varepsilon_a - \varepsilon_b$ also decreases. The rationale for the latter assertion is that, at some threshold doping concentration, stripes should disappear, which implies that holes

should be expelled from them. According to Eqs. (46) or (63), the decrease of the pseudogap is accompanied by the increase of the critical temperature.

The interaction strength g should also change with the increase of doping. It is not obvious *a priori* whether it increases or decreases, but, at least, it is likely that the value of g never approaches zero, while the value of $\varepsilon_a - \varepsilon_b$ either reaches zero at some critical doping or becomes very small. This suggests that the relative change of $\varepsilon_a - \varepsilon_b$ across the SC doping range has stronger effect on the observable quantities than the relative change of g.

If the value of g were independent of the doping concentration, then the maximum of T_c would be achieved at a critical doping corresponding to $\varepsilon_a - \varepsilon_b = 0$. However, because of the presumed dependence of g on the doping level, the optimal doping concentration, x_{d0}, corresponding to the actual maximum of T_c, can be slightly shifted with respect to the critical one. The comparison with experiments in Sec. VIII D indicates that the above notion of the critical doping coincides with the "critical doping" $x_{dC} \approx 0.19$ identified experimentally in Refs.[51–53] As expected, $x_{d0} \approx 0.16$ is not much different from x_{dC}. The fact that $x_{d0} < x_{dC}$ suggests that g decreases as the doping level increases.

Below the critical doping, the inequality $\varepsilon_a > \varepsilon_b$ implies that the real materials can be describable by the model either as Case IA or as Case IIB (see Sec. VIII E for the discussion of this issue).

Above the critical doping, it is, in principle, possible that either $\varepsilon_a - \varepsilon_b$ stays equal to zero, while only g changes, or $\varepsilon_a - \varepsilon_b$ becomes negative, which means that the absolute value of the "inverted" pseudogap starts growing again and thus additionally suppresses the critical temperature. The analysis of experiments in Sec. VIII D favors the inverted pseudogap scenario and, given the model choice between Cases IB and IIA, clearly points to Case IB. As discussed in Sec. V, the stripe superstructure may, for a while, remain stable even after ε_b becomes greater than ε_a. It is further possible that the SC transition can contribute to the stabilization of stripes by lowering the total energy of the stripe phase.

In the context of the present proposal, stripes should exist in the SC phases of both underdoped and overdoped cuprates. It is, however, unclear, whether, in overdoped cuprates, stripes can be stabilized without the SC transition. Negative answer to this question would imply that above the SC transition, overdoped cuprates enter a stripeless normal state. Otherwise, the normal state of overdoped cuprates may still exhibit some kind of stripe order. In turn, if overdoped cuprates enter stripeless phase simultaneously with the SC transition, then this important aspect cannot be captured by the model of Sec. VI. In such a case, the model scenario for the overdoped situations becomes doubtful.

The conceptual difference between the above description and the popular idea of competing orders is that, in the present proposal, the two orders are not competing, but, on the contrary, cooperating: the stripe order is crucial for the existence of the SC transition, while the SC transition can also help stabilizing the stripe order.

VIII. COMPARISON WITH EXPERIMENTS

A. Qualitative aspects

The primary concern in the context of the present proposal is that no evidence of stripes has been observed so far in most optimally doped and overdoped materials. It should be pointed out, however, that this proposal stipulates that strong transverse fluctuations of stripes mediate superconductivity. If true, this would imply that any attempt to observe stripes by pinning charges or freezing spins, would suppress their transverse fluctuations, and thus suppress the SC transition or, at least, significantly reduce the critical temperature. Such an inverse relation between the amplitude of the stripe fluctuations and T_c can explain why the stripes are best observable in cuprates having lower T_c, such as underdoped,[34,46] Nd-doped[44] and Zn-doped[45–47] LSCO. The transverse fluctuations of stripes should be strongly coupled to the lattice. Therefore, some kind of isotope effect should also be present in such a system.

The proper treatment of the single particle excitations in the nonsuperconducting (normal) 2D stripe phase is not developed in this work. It is, however, difficult not to see that the description of the normal state pseudogap given in Sec. V, while following only from the basic facts about the 2D stripe geometry, bears a strong resemblance to the experimental facts.[17] In particular, the disappearance of the pseudogap in the diagonal crystal directions can be naturally explained by the presence of holes inside the diagonal stripes. In the model framework, the absolute value of the pseudogap $|\varepsilon_a - \varepsilon_b|$ constitutes the primary factor suppressing the SC transition [see Eqs. (46) and (63)].

In the SC state, the model predicts such distinctive properties as (i) the suppression of T_c with the growth of the pseudogap $|\varepsilon_a - \varepsilon_b|$ [see Eqs. (46) and (63)]; (ii) the emergence of quasiparticles having coherent dispersion in k-space only at $T < T_c$ [see the remark following Eq. (27)]; (iii) the asymmetry of the tunneling density of states [Fig. 7(a)]; (iv) linear density of states around the chemical potential (Figs. 7(b) and 7(c)); and (v) low superfluid density (Sec. VI F). In the following subsections VIII B–VIII D), I show that some of the quantitative model predictions made without adjustable parameters also agree with experiments.

B. Tunneling characteristics

In this subsection I compare the theoretical tunneling spectra at $T = 0$ with experimental tunneling spectra at $T \ll T_c$. Therefore, the discussion will imply the zero-temperature values of all relevant quantities.

The model predicts two kinds of contributions to the tunneling density of states corresponding to A- and B- Bogoliubov quasiparticles (see Fig. 7). If the Van Hove singularities at $\pm\varepsilon_{A0}$ and the delta-function peaks at $\pm\varepsilon_B$ exist at all, they should be identifiable in experimental data.

The difficulty now is that the tunneling spectra of high-T_c cuprates have, in general, only one prominent feature, namely, two SC peaks at the opposite values of the bias. The energies of the SC peaks are, usually, denoted as $\pm\Delta$, and Δ is referred to as the SC gap. In the superconductivity model of Bardeen, Cooper and Schrieffer (BCS), $\Delta/T_c = 1.76$. In

high-T_c cuprates, the reported values of Δ/T_c show significant variations but, typically, fall in the range between 1.5 and 7, with 4 being a representative value. In the present model, the ratios $|\varepsilon_{A0}|/T_c$ and $|\varepsilon_B|/T_c$ can also vary broadly. Their representative values are 4 and 1, respectively (see Sec. VI G). Having observed that $\Delta/T_c \sim |\varepsilon_{A0}|/T_c$, I identify the experimental SC peak with the Van Hove singularity in the density of *A*-states. This identification will later prove to be consistent with a number of other qualitative and quantitative facts. In the following, the variables $|\varepsilon_{A0}|$ and Δ will refer, respectively, to the theoretical and experimental values of the same quantity.

The identification of *B*-states is more problematic. The evidence for their existence is nontrivial, but largely indirect. It is based on the STM observations of the checkerboard patters in the local density of states (LDOS) of Bi-2212[18–21] (to be discussed in subsection VIII C). Another possibly related observation is that of asymmetric resonance peaks in YBCO by Derro *et al.* The asymmetry and the energy range of those peaks agree well with the expectations for the delta peaks due to *B*-states [see Fig. 7(c)].

There are two possible explanations why, in general, *B*-states are more difficult to observe experimentally.

The first explanation is that, in a real system, the on-site energies ε_b can be distributed. As a result, the spectrum of *B*-states may become broad and featureless.

The second explanation is that the matrix elements for tunneling into *b*-states (and hence *B*-states) can be much smaller than those for *a*-states. This, in turn, can be related to the fact that *b*-states are localized in the narrow regions inside the stripes, while *a*-states spread over the AF domains and thus have a broader "interface" with the environment. Alternatively, it might happen that *b*-states have exotic quantum numbers, in which case tunneling into them can be suppressed at all.

In the rest of this subsection, I assume that *B*-states are mostly unobservable, and, unless specified otherwise, the tests of the model will amount to the comparison between the density of *A*-states and the experimental tunneling spectra.

I limit the choices to the special Cases I and II defined in Sec. VI B. Therefore, the model calculation of the density of *A*-states only requires the knowledge of two parameters: g and ε_a in Case I, or g and ε_b in Case II. Using T_c and Δ as input parameters, I can both discriminate between Cases I and II, and determine the values of g, ε_a and ε_b.

The inequality $\Delta/T_c > 4$ can appear only in the framework of Case I, in which case, $|\varepsilon_a|$ and g should be obtained numerically from Eqs. (46) and (50) (with $n_B=1$ and $\varepsilon_{A0}=\Delta$). The opposite inequality, $\Delta/T_c < 4$, can only correspond to Case II, i.e., $|\varepsilon_b|$ and g have to be obtained from Eqs. (60), (63), and (65) (with $n_B=0$, $C_a=C_{a0}$ and $\varepsilon_{A0}=-\Delta$). The situation $\Delta/T_c=4$ corresponds to the critical case described in Sec. VI G.

After the model Hamiltonian is specified, the following tunneling characteristics can be predicted without adjustable parameters: (i) the asymmetry in the density of *A*-states or the absence thereof, (ii) the maximum energy of *A*-states ε_{A1}, and also (iii) the expected positions $\pm\varepsilon_B$ of the delta-peaks representing *B*-states.

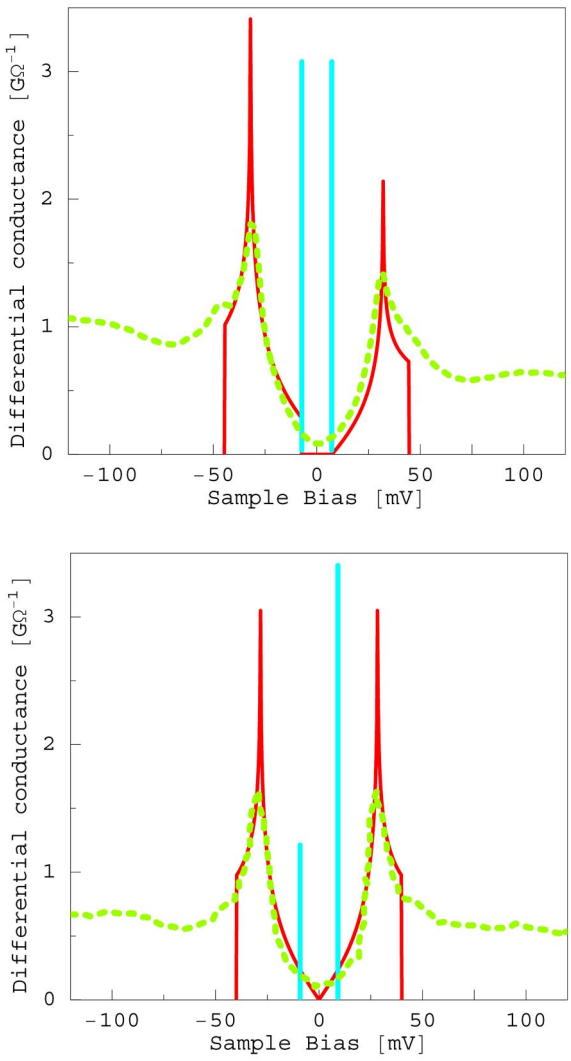

FIG. 12. (Color online) Comparison between zero-temperature model calculations and low-temperature STM spectra of Bi-2212. Solid lines represent the theoretical density of states in the same way as in Fig. 7. Dashed lines represent experimental spectra extracted from the following references: (a) Fig. 2 of Ref. 54 (regular part of Bi-2212 surface); (b) Fig. 7 of Ref. 55.

The selection of Case I implies a strong qualitative prediction of asymmetric SC peaks. However, the knowledge of Δ and T_c alone cannot help to discriminate between Cases IA and IB, which correspond to the opposite "polarities" of the SC peak asymmetry. However, if Case I is identified in underdoped cuprates, then the strong expectation is that $\varepsilon_a > \varepsilon_b$, which implies Case IA (larger SC peak at the negative bias). The identification of Case II implies that the SC peaks are symmetric. (The inequality $\varepsilon_a > \varepsilon_b$ would then favor Case IIB for underdoped cuprates.)

In Fig. 12, the model calculations are compared with two particularly well resolved STM spectra of Bi-2212. The experimental spectrum in Fig. 12(a) was extracted from Fig. 2 of Ref. 54. It is representative of "regular" parts of the sample surface (i.e., vortex free and impurity free). In this case, the experimentally determined numbers $\Delta=32$ meV, $T_c=87$ K and $\Delta/T_c=4.3$ imply Case I with $|\varepsilon_a|=7.3$ meV

and $g=31$ meV. The theoretical spectrum presented in Fig. 12(a) corresponds to $\varepsilon_a>0$, i.e., to Case IA.

The experimental spectrum in Fig. 12(b) was extracted from Fig. 7 of Ref. 55. The relevant experimental numbers $\Delta=28$ meV, $T_c=92.3$ K and $\Delta/T_c=3.5$ imply Case II with $|\varepsilon_b|=4.3$ meV and $g=32$ meV. The asymmetry of the theoretical delta-peaks in Fig. 12(b) corresponds to $\varepsilon_b<0$, i.e., to Case IIB. The vertical scale of the theoretical plots in Fig. 12 was chosen to fit best the experimental data.

It thus appears, that not only does the model give the correct prediction of the presence or the absence of the SC peak asymmetry, but also it predicts the degree of asymmetry quantitatively. One should also note that the termination points of the theoretical spectra have experimental counterparts in the form of the shoulder-like features located approximately at energies $\pm\varepsilon_{A1}$ predicted theoretically. Finally, the delta-peaks shown in Fig. 12(a) are located at $\pm\varepsilon_B=\pm 7.3$ meV. These are precisely the energies, at which, in Ref. 54, the vortex cores have shown anomalous *symmetric* "humps" absent in the regular SC regions. The local density of states (LDOS) associated with the above humps was later shown to exhibit a checkerboard pattern inside the vortex cores.[18] In subsection VIII C, I will show that this pattern is precisely what one should expect from LDOS associated with *B*-states.

Now I discuss to what extent the model-based rule

$$\text{"}\Delta/T_c>4 \Leftrightarrow \textit{asymmetric SC peaks};$$

$$\Delta/T_c\leqslant 4 \Leftrightarrow \textit{symmetric SC peaks"} \qquad (103)$$

is supported by other STM or point-contact superconductor—insulator—normal-metal (S-I-N) experiments. The values of Δ used below are obtained as half of the difference between the energies of the SC peak maxima.

Supporting evidence:

Clearly asymmetric SC peaks corresponding to $\Delta/T_c>4$ have been reported for bilayer compounds

Bi-2212 in Refs. 54 and 56–62,

$HgBa_2CaCu_2O_{6+\delta}$ (Hg-1212) in Ref. 63;

and trilayer compounds

$Bi_2Sr_2Ca_2Cu_3O_{10+\delta}$ (Bi-2223) in Ref. 64,

$HgBa_2Ca_2Cu_3O_{8+\delta}$ (Hg-1223) in Refs. 63 and 65.

The values of Δ/T_c extracted from the above references cover the range between 4.1 and 6.9.

Symmetric SC peaks corresponding to $\Delta/T_c\leqslant 4$ have been reported for single layer compounds

$HgBa_2CuO_{4+\delta}$ (Hg-1201) in Refs. 63 and 64,

$Tl_2Ba_2CuO_6$ (Tl-2201) in Ref. 66;

and bilayer compounds

Bi-2212 in Refs. 55 and 56, also Pb-doped Bi-2212 in Ref. 67,

YBCO in Ref. 68,

$Tl_2Ba_2CaCu_2O_x$ (Tl-2212) in Ref. 69.

The values of Δ/T_c extracted from the above references cover the range between 1.7 and 3.9.

Contradicting evidence:

Symmetric SC peaks corresponding to $\Delta/T_c>4$ have been reported for

Bi-2212 in Refs. 55, 59, 60, and 70.

Asymmetric SC peaks corresponding to $\Delta/T_c\leqslant 4$ have been reported for

LSCO in Ref. 71,

Tl-2201 in Ref. 66,

Tl-2212 in Ref. 69.

However, in the case of LSCO, the difference between the peak heights was certainly within the limits of experimental uncertainty. In the case of Tl-2201 and Tl-2212, the overall impression from the cited references is that the SC peaks are largely symmetric. (Most of the spectra reported in the same references and measured on similar junctions pass as symmetric and contribute to the "supporting evidence.")

Unlike the two spectra shown in Fig. 12, most of the measured tunneling spectra have more rounded SC peaks, which may be the consequence of limited experimental resolution. Since a significant broadening of a SC peak also shifts the position of its maximum, it is possible that, a measured symmetric spectrum indicates the ratio Δ/T_c greater than 4, while the true ratio Δ/T_c is slightly smaller than 4. (One such an example is given in Ref. 55.) The resolution-limited broadening of the SC peaks can, therefore, be responsible for at least a part of the "contradicting evidence" in Bi-2212.

Taken as a whole, the above review of experimental data clearly supports the rule (103). Furthermore, this rule (103) seems to unify the experimental data, which, otherwise, may appear contradicting to each other. (I will return to this issue in Sec. VIII E.)

Another interesting fact is that, in the references cited above, the SC peak asymmetry of the bilayer compounds is opposite to that of the trilayer compounds: the bilayer compounds have the higher SC peak mostly at the negative bias [as in Fig. 12(a)], while the trilayer compounds have the higher peak at the positive bias.

Rule (103) can be compared with a more simple prediction made by Altman and Auerbach,[28] that the asymmetry of the kind shown in Fig. 12(a) is inherent in all high-T_c cuprates. The lack of the asymmetry in some of the tunneling spectra and the opposite asymmetry of the tri-layer compounds would contradict to the above prediction.

Finally, one additional clear prediction of the model is that the inequality $\Delta/T_c>4$ implies that, as T approaches T_c, the energy of the SC peaks approaches the finite value $|\varepsilon_a|$ [see Eq. (50)]. The inequality $\Delta/T_c<4$ implies the zero energy of the SC peaks at $T=T_c$ [see Eq. (65)]. The above prediction is difficult to test, because the SC peaks tend to be totally "washed out" in the vicinity of T_c. Nevertheless, one can observe that the first part of this prediction is consistent with the trend in the tunneling data from Refs. 59 and 72–75. The second part is more difficult to test, but it also appears to be consistent with the results reported in Refs. 74, 76, and 77, though the results from Refs. 73 and 75 leave either ambiguous or the opposite impression.

C. *B*-states and the checkerboard patterns observed by STM

The only experimental evidence, which, at the moment, I can identify with *B*-states is the checkerboard modulation of the LDOS observed by STM in the vortex cores.[18] The analogous modulations observed in the normal state of

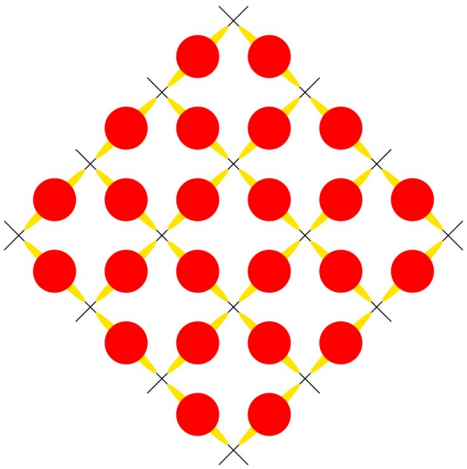

FIG. 13. (Color online) Checkerboard pattern formed by the centers of stripe elements. Circles indicate the regions, where the densities of *B*-states in the SC phase or *b*-states in the normal phase are expected to be particularly high.

Bi-2212[21] can be attributed to *b*-states. [For the alternative interpretations of these (and other) checkerboard patterns see Refs. 11, 19, 20, 31, and 78–82].

The checkerboard modulations revealed by the above experiments have periodicity of approximately four lattice periods along the principal lattice directions. From the viewpoint of the present proposal, this periodicity is due to the response from *B*-states in the SC state or *b*-states in the normal state. These model states are localized around the centers of the stripe elements, which, as shown in Fig. 13, form a pattern with the required orientation of the "checkerboard."

As a corroborating evidence, I can mention that, in the vortex core experiments,[18,54] the LDOS modulation was most pronounced at energies approximately equal to ± 7 meV, in almost exact correspondence with $\pm\varepsilon_B$ obtained in Sec. VIII B just from the knowledge of Δ and T_c for the spectrum presented in Fig. 12(a). In the normal state experiment,[21] the typical range of energies, where the modulations were most pronounced, was also consistent with the possible energies of *b*-states.

In regular SC regions of nearly optimally doped Bi-2212, a different kind of LDOS modulations showing strong energy dependence has also been observed.[19,20] From the viewpoint of the present proposal, this energy dependence can be caused by two factors: (i) the crossover from the pattern corresponding to *B*-states to the pattern corresponding to *A*-states; and (ii) the defect-induced interference of *A*-quasiparticles. The first factor can be appreciated after one observes that the spatial patterns of *A*-states and *B*-states are characterized by different sets of wave vectors. The pattern of *A*-states has diagonal periods ℓ coinciding with that of the underlying stripe superstructure, while the periods of *B*-states (shown in Fig. 13) are equal to $\ell/\sqrt{2}$ and oriented along the principal lattice directions. Therefore, as the energy probed by STM increases, the pattern representative of *B*-states gradually transforms into the pattern representative of *A*-states, hence the energy dependence of the characteristic wave vectors. The description of the second (interference) factor would require quantitative analysis extending beyond the scope of the present work. (The idea, that a different kind of the quasiparticle interference can entirely explain the energy-dependent modulation patterns, was advocated in Refs. 20 and 80).

Since, in the 2D diagonal stripe picture, the experimentally observed checkerboard periodicity of $4a_0$ implies the true underlying period $\ell = 4a_0\sqrt{2}$ along the diagonal directions, a direct test for the existence of the diagonal superstructure can consist of reconstructing the position of hypothetical diagonal stripes from the knowledge of the checkerboard pattern at lower energies, and then checking whether the LDOS modulation at higher energies has more pronounced correlations between the (approximately) equivalent positions belonging to different supercells.

Finally, the in-stripe hole content corresponding to the present interpretation can be estimated by substituting $x_d \approx 0.16$ and $f = a_0\sqrt{2}/\ell = 1/4$, into Eq. (4), which gives $c = x_d/f = 0.6$. This number is only slightly greater than 0.5 extracted in Sec. II from the experimentally observed INS peak splitting in underdoped LSCO compounds.

D. Superfluid density

In the model framework, the calculation of the critical temperature T_c and the superfluid density, S_ϕ, requires the knowledge of three numbers: $|\varepsilon_a - \varepsilon_b|$, g and the prefactor of S_ϕ. In general, one should expect that both $|\varepsilon_a - \varepsilon_b|$ and g change as functions of doping concentration. However, since $|\varepsilon_a - \varepsilon_b|$, presumably, approaches zero not far from the optimal doping, the relative effect of this change on the observable quantities should be stronger than the effect of the change of g. Therefore, for a given family of high-T_c cuprates, one can obtain an approximate relation between S_ϕ and T_c by fixing the value of g and then varying ε_a in Case I or ε_b in Case II. The two theoretical curves shown in Fig. 10 were obtained precisely in this way.

In this subsection, I test the model relationship between S_ϕ and T_c by superimposing the (rescaled) theoretical plot of Fig. 10 on the experimental results for Tl-2201,[83–85] $Tl_{0.5-y}Pb_{0.5+y}Sr_2Ca_{1-x}Y_xCu_2O_7$ (Tl-1212),[51] Hg-1201,[86] LSCO,[53,87] Bi-2212,[53] Ca-doped YBCO (Y:Ca-123)[53] and YBCO,[88] which report either relaxation rate σ measured by muon spin rotation (μSR) technique, or the inverse square of the penetration depth λ extracted from the μSR data, field-dependent thermodynamic measurements, or electron spin resonance studies. Both σ and λ^{-2} should be proportional to S_ϕ. The result is shown in Figs. 14 and 15.

In each of Figs. 14(b)–14(f), the theoretical plot is rescaled in such a way that the critical case point (the one, where the dashed and the solid curves intersect) coincides with the experimental critical point. The latter is defined as the point where the derivative of the experimental T_c vs S_ϕ dependence undergoes an apparent discontinuous change. In Refs. 51–53, the same point was found to correspond to the so-called "critical doping concentration" approximately equal to 0.19. In Figs. 14(g) and 14(h) the theoretical critical point simply matched the experimental point of the maximal superfluid density. (Here I ignored the issue of anisotropy

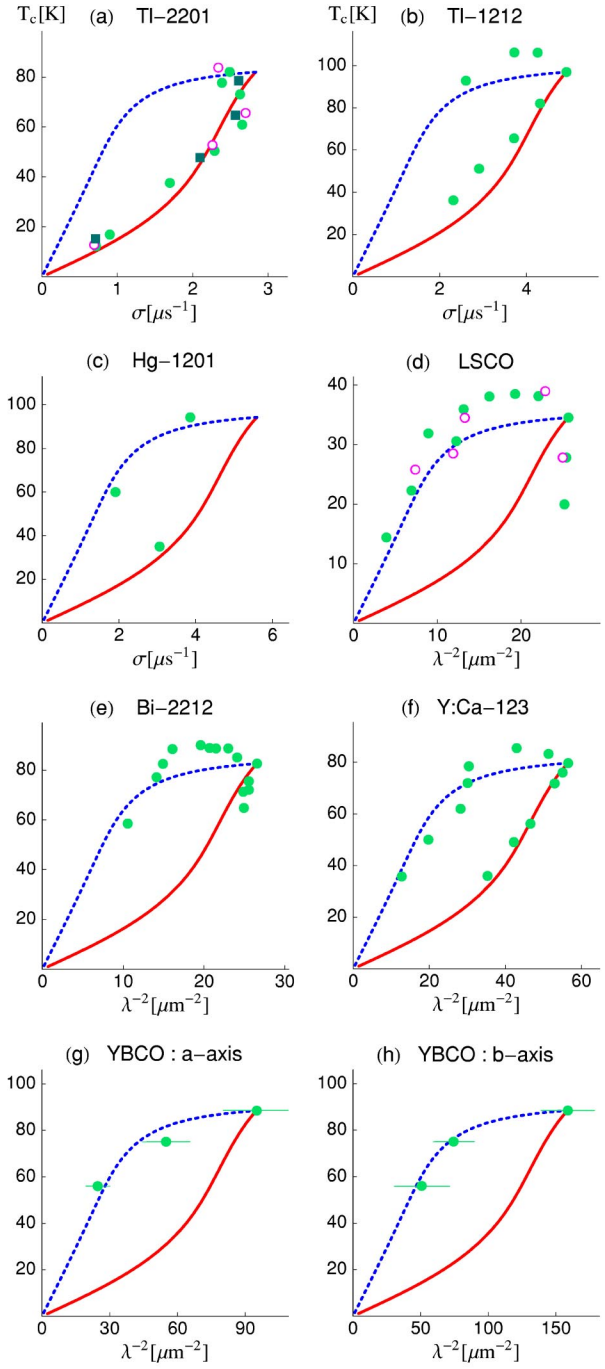

FIG. 14. (Color online) Critical temperature vs superfluid density (presented as σ or λ^{-2}) at $T \cong 0$. The theoretical plots (solid and dashed lines) are obtained by simple rescaling of the plot presented in Fig. 10. The experimental points are extracted from the following references: (a) filled circles—Ref. 85, open circles—Ref. 84, squares—Ref. 83; (b) Ref. 51; (c) Ref. 86; (d) filled circles—Ref. 53, open circles—Ref. 87; (e, f) Ref. 53; (g, h) Ref. 88. The doping ranges corresponding to the experimental points are shown in Fig. 15.

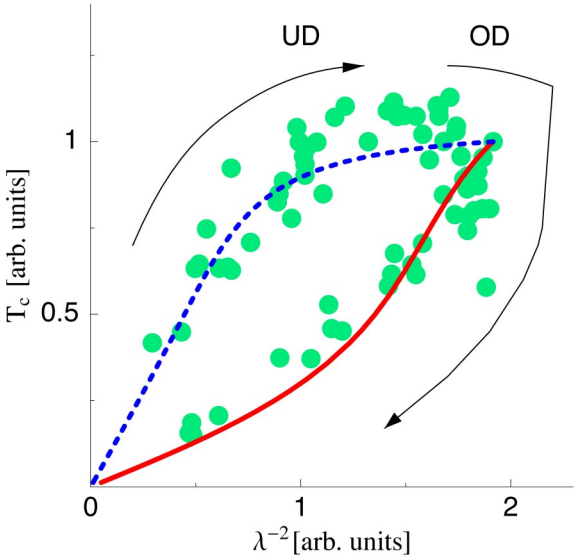

FIG. 15. (Color online) All the data points from Fig. 14 rescaled in such a way that the theoretical plots coincide with each other. The arrows indicate the direction, in which the doping concentrations increase. "UD" and "OD" indicate underdoped and overdoped samples, respectively.

and treated *a*-axis and *b*-axis data as independent data sets.) In Figs. 14(a) and 14(c), the rescaling relied on the overall best fit to the experimental data rather than on matching a specific point.

The comparison with experiments in Fig. 14 amounts to the following (crude) quantitative test of the model: After the interaction constant g and the prefactor of S_ϕ are fixed by establishing the absolute scale for the theoretical critical point, the values of *two* independent numbers S_ϕ and T_c for noncritical points are obtained by varying only *one* theoretical parameter: ε_a in Case I or ε_b in Case II.

As is evident from Figs. 14 and 15, the theoretical "fish-like" plot clearly captures the main features of the experimental data, namely: the existence of two different regimes, with a critical point of the maximal superfluid density separating them. The quality of the quantitative agreement in Figs. 14(a) and 14(f) is particularly surprising, given the crudeness of the test and the fact that the data extend into the overdoped region, where the model assumptions appear less reliable *a priori*.

At the point corresponding to the critical case, one can also estimate the absolute value of the penetration depth from Eq. (101). This estimate, which only requires the knowledge of the critical temperature and the transverse distance per one CuO_2 plane, was made in Sec. VI G with the numbers close to those of YBCO or Bi-2212. The number obtained ($\lambda = 417$ nm) is about 3–4 times greater than the numbers typically cited for YBCO (see, e.g., Ref. 88) and about two times greater than the numbers cited for Bi-2212 (see, e.g., Ref. 53). This comparison is representative of the general trend: the theoretical formula (101) overestimates the penetration depth by about a factor of 3.

For a simple estimate, which involves only the fundamental constants and two well-known material parameters (T_c and z_0), the factor-of-3 agreement with the experimental numbers is quite reasonable. One should also be conscious of

the possibility (mentioned in Sec. VI F) that the profile of magnetic field may strongly fluctuate within the penetration depth layer. At the same time, the absolute values of the penetration depth are typically extracted from the experimental data on the basis of theoretical formulas, which do not take into account such a possibility.

E. Correspondence between the model regimes and the doping concentrations

In this subsection, I attempt to establish the correspondence between model Cases IA, IB, IIA and IIB and the doping concentrations of high-T_c cuprates. On the basis of the content of Secs. V, VIII B, and VIII D, the following four criteria discriminating between the four model Cases can be proposed:

Criterion 1: The inequality $\Delta/T_c > 4$ indicates Case I, while $\Delta/T_c < 4$ indicates Case II.

Criterion 2: When the theoretical fish plot from Fig. 10 is superimposed on the experimental dependence of T_c on the superfluid density, the proximity of a data point to the solid line indicates Case I, while the proximity to the dashed line indicates Case II.

Criterion 3: The asymmetry in the tunneling density of states characterized by a larger SC peak at negative voltages indicates Case IA. The opposite asymmetry indicates Case IB.

Criterion 4: When the asymmetry in the tunneling density of states is not accessible, I will rely on the postulate, that, in underdoped cuprates, $\varepsilon_a > \varepsilon_b$, which favors Case IA over IB, and IIB over IIA.

Criterion 2, when applied to Fig. 15, suggests a very simple picture: The cuprates are describable by Case II at subcritical doping concentrations $x_d < x_{dC} \approx 0.19$, and by Case I at the supercritical concentrations $x_d > x_{dC}$. *Criterion 4* then further narrows the choice to Case IIB for $x_d < x_{dC}$. This identification implies that, at low doping, $\mu = \varepsilon_a > \varepsilon_b$, and then, as the doping concentration increases, the difference $\varepsilon_a - \varepsilon_b$ decreases until, at the critical doping, it becomes equal to zero. The identification of Case I for $x_d > x_{dC}$ then suggests that $|\varepsilon_a - \varepsilon_b|$ starts increasing again (but now with $\mu = \varepsilon_b$). Since the derivative of $\varepsilon_a - \varepsilon_b$ as a function of doping is unlikely to change sign exactly at $x_d = x_{dC}$, I conclude that the model pseudogap $\varepsilon_a - \varepsilon_b$ *changes sign* as x_d passes x_{dC}. This means that, at the supercritical doping concentrations, $\varepsilon_a < \varepsilon_b$, which implies Case IB. Thus the assignment following from the above discussion is

$$x_d < x_{dC} \Rightarrow \text{Case IIB},$$

$$x_d > x_{dC} \Rightarrow \text{Case IB}. \qquad (104)$$

The clear systematics of the superfluid density data should now be contrasted with a less systematic picture emerging from the tunneling data.

Most of the point-contact and STM tunneling spectra discussed in subsection VIII B, as well as break junction and interlayer tunneling spectra, are collected at doping concentrations $x_d \leqslant x_{dC}$. In this doping range, the tunneling data for Tl-2201,[66] $Tl_2Ba_2CaCu_2O_{8+\delta}$ (Tl-2212),[69] Hg-1201,[63,64] LSCO,[71] YBCO[68,89,90] (and also $YbBa_2Cu_3O_{7-x}$[89,90]) support inequality $\Delta/T_c \leqslant 4$, which, according to *Criterion 1*, suggests Case II in agreement with the assignment (104).

The tunneling studies of Bi-2212 do not reveal a coherent picture either in terms of the ratio Δ/T_c or in terms of the SC peak asymmetry. Most of more recent Bi-2212 tunneling data for $x_d \leqslant x_{dC}$[54,58–61,70,72–74,91] show $\Delta/T_c > 4$, and whenever the asymmetry is evident in the data, it mostly points to Case IA—in clear contradiction with the assignment (104). At the same time, many other (and some of the same) tunneling studies[55,56,67,74,76,92] find in the same doping range the gap values corresponding $\Delta/T_c \leqslant 4$ and thus, according to *Criterion 1* support the assignment (104).

The remarkable fact is that, at least on two occasions,[56,57,74] the tunneling spectra of Bi-2212 presented in the same paper and measured on samples with nearly equal critical temperatures have shown two different values of Δ/T_c—one significantly greater than 4, and the other one smaller than 4.

The tunneling phenomenology of Bi-2212 can be explained by the existence of two different SC states, which, for $x_d < x_{dC}$, correspond either to Case IA or to Case IIB. As argued in Sec. VI D, both SC states are characterized by sharp minima of the total energy of the system and by the same critical temperature. One of them can, e.g., constitute a stable bulk state, while the other one a stable or metastable surface state.

The asymmetric STM spectrum of Hg-1212 reported in Ref. 63 clearly suggests Case IA, which cannot be placed within the assignment (104).

Criteria 1 and *3*, when applied to the asymmetric STM spectra for the trilayer compounds Bi-2223[93] and Hg-1223[63] suggest Case IB, and thus could be compatible to the assignment (104) provided that the doping concentration in those samples exceeds the (unknown) critical concentration for the corresponding families of cuprates. However, the recent interlayer tunneling results for Bi-2223[75] indicate that, as the doping concentration increases, the ratio Δ/T_c decreases from values larger than 4 to values smaller than 4, which, in combination with the STM data,[93] rather suggests the assignment opposite to (104), namely: Case IB for $x_d \leqslant x_{dC}$ and Case IIB for $x_d > x_{dC}$.

Summary of the findings of this subsection: Assignment (104) is consistent with the superfluid density data and/or the tunneling data reported for Tl-2201, Tl-2212, Tl-1212, Hg-1201, LSCO and YBCO. For Bi-2212, the same assignment is partially supported by experiments, while the overall phenomenology rather suggests the occurrence of two different SC states at the same doping concentration. The limited tunneling data on Hg-1212, Hg-1223 and Bi-2223 appear to contradict to the assignment (104) with varying degrees of certainty. Assignment (104), if true, implies that the pseudogap changes sign at the critical doping concentration.

F. Symmetry of the SC order parameter

The prediction, which distinguishes the present proposal from many others, is the nontrivial translational symmetry of the SC order parameter. This property has not yet been in-

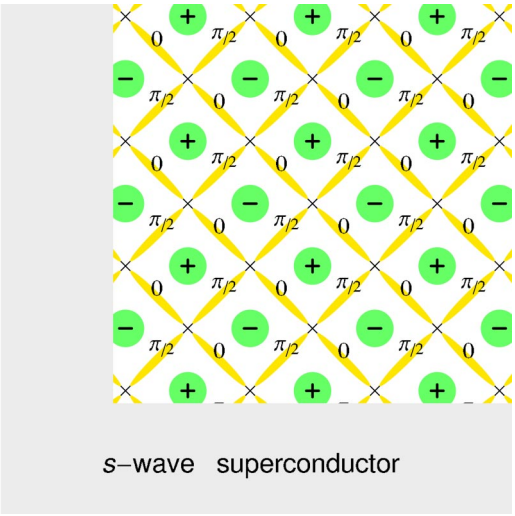

FIG. 16. (Color online) Possible geometry of a corner SQUID experiment.

vestigated experimentally. One straightforward experimental test would be to construct a nanoscale probe, which is sensitive to the SC phase difference between two points separated by one period of the expected stripe superstructure. Slightly prior to the appearance of the present work, the position-dependent sign change of the SC order parameter has also been proposed by Ashkenazi[29] in the context of a different stripe-related model.

An important question is whether the SC order parameter introduced in this work is consistent with the phase sensitive experiments, which are usually interpreted as the evidence for $d_{x^2-y^2}$ symmetry of a spatially uniform SC state (see, e.g., Ref. 94). Here I am primarily concerned with the corner superconducting quantum interference device (SQUID) experiments[95] and with the tricrystal junction experiments.[96,97]

A definitive discussion of these experiments cannot be given at this time because of the following two uncertainties:

(i) The continuous family of possible SC solutions obtained in Sec. VI C has not been narrowed to a single one.

(ii) The boundary conditions necessary for the discussion of the phase sensitive experiments have not been specified.

In view of the above uncertainties, I limit further discussion to presenting just one of several possible interpretations of the well-known π phase shift observed in the corner SQUID experiments.[95] This interpretation is illustrated in Fig. 16. It is based on the same SC phase pattern as the one shown in Fig. 6(a). The examination of Fig. 16 reveals that the phases "0" and "$\pi/2$," which characterize both Ψ_a and Ψ_b, form the same pattern along both of the SQUID interfaces, which means that this aspect of the phase symmetry is unlikely to contribute to the relative phase shift between the two interfaces. However, in addition, the Ψ_a component also has the position dependent sign factor, which is indicated in the centers of the supercells as "+" or "−." The important fact is that, despite the sign change of Ψ_a, the Josephson coupling between Ψ_a and the order parameter of the conventional superconductor is not averaged to zero along each of the two interfaces shown in Fig. 16. Now I assume that, at these interfaces, the order parameter of the conventional superconductor preferentially couples to Ψ_a (as opposed to Ψ_b). In such a case, the opposite signs of Ψ_a along the two interfaces imply the required phase shift of π.

The interpretation of the tricrystal experiments,[96,97] in which vortices carrying half of the flux quantum were observed, is not practical at this time, because it should depend critically on the unknown boundary conditions. Here, I can only mention, that, the design geometry of the tricrystal experiments is such that, if the postulated 2D stripe superstructure exists in each of the three adjacent crystals, then the three interfaces between the intersecting stripe superstructures are nearly equivalent to each other. Therefore, the explanation of these experiments will likely amount to showing that each of the junctions generates a π phase shift.

Finally, I discuss the observation of the *c*-axis Josephson pair tunneling between YBCO single crystals and the films of Pb.[98] (Pb is a conventional s-wave superconductor.) This experimental fact is difficult to explain on the basis of the "*d*-wave" picture.[94] At the same time, in the framework of the present proposal, it can be easily interpreted as follows: When a conventional superconductor is placed on the top of the 2D striped system shown in Fig. 16, the contribution of the Ψ_a component to the Josephson coupling changes sign and thus averages to zero, but the contribution from the Ψ_b component, which does not change sign, can lead to a finite Josephson current.

IX. CONCLUSIONS

In the present work, I have analyzed several consequences of the hypothesis that holes doped into high-T_c cuprates organize themselves in two-dimensional arrays of deep stripes. In particular, on the basis of this hypothesis, I have formulated and solved a model of superconductivity. From that model, I have obtained the tunneling spectrum and the superfluid density, which show good agreement with experiments. The symmetry of the SC order parameter derived from the model is different from that of $d_{x^2-y^2}$ BCS order parameter. The order parameter obtained in this work has two components, at least one of which changes sign as a function of the absolute position of the pair on the spatial scale of the stripe superstructure. A number of other features of this proposal such as the geometry of the pseudogap and the effect of the pseudogap on the superconducting transition temperature appear to be in qualitative agreement with the phenomenology of high- T_c cuprates. The checkerboard pattern of LDOS observed by STM has been interpreted as coming from the centers of stripe elements in the 2D arrangement of diagonal stripes. This work also indicates the possibility, that, in underdoped cuprates, there may exist two different kinds of SC states, and that, at the critical doping concentration, the pseudogap may change sign.

Even if a future work demonstrates the inadequacy of the theoretical assumptions of the present one, the systematics of the asymmetry in the tunneling spectra discussed in Sec. VIII B and the scaling of the superfluid density data shown in Fig. 15 should retain the status of useful empirical facts.

ACKNOWLEDGMENTS

The author is grateful to M. Turlakov, A. J. Leggett, R. A. Klemm, P. Fulde, K. Maki, B. Altshuler, P. McHalle, V. Krasnov, J. C. Davis, C. Panagopoulos, L. P. Gor'kov, J. Zaanen, and J. M. Tranquada for helpful discussions.

APPENDIX A: APPROXIMATE SOLUTION VIA A NONCANONICAL TRANSFORMATION

In this appendix, I present an approximate scheme of finding the variational ground state of Hamiltonian (7) using the following Bogoliubov-like *noncanonical* transformation of *a*-states *in real space*

$$a_i = uA_i + v\,\eta_i \sum_{j(i)} A_j^+ \tag{A1}$$

together with regular Bogoliubov transformation of *b*-states

$$b_{ij,+} = sB_{ij,+} + wB_{ij,-}^+, \tag{A2}$$

$$b_{ij,-} = sB_{ij,-} - wB_{ij,+}^+, \tag{A3}$$

where A_i and $B_{ij,\sigma}$ are the annihilation operators of the Bogoliubov quasiparticles; u, v, s and w are the transformation coefficients. These coefficients can be chosen real. They must then obey the following normalization constraints:

$$u^2 + 4v^2 = 1, \tag{A4}$$

$$s^2 + w^2 = 1. \tag{A5}$$

(Variables u and v of this appendix should not be confused with functions $u(\mathbf{k})$ and $v(\mathbf{k})$ defined by Eqs. (25) and (26).

The second term on the right-hand side of Eq. (A1) changes sign from supercell to supercell following the sign of η_i. This sign change is necessary to ensure that the canonical fermionic anticommutation relations between operators A_i and A_j corresponding to neighboring AF domains are not violated in the first order of v. This transformation is still noncanonical, because it violates the anticommutation relations in the second and higher orders of v. In order to see this, one can assume that *A*-operators represent true fermions and then check the anticommutation relation between operators a_i and a_p^+ corresponding to a pair of next nearest neighbors.

Despite the fact that transformation (A1) is not canonical, I will substitute it (together with transformations (A2) and (A3), into the Hamiltonian (7) and then handle *A*-operators as if they were true fermionic operators.

The justification for such a scheme is threefold: (i) The noncanonical transformation (A1) is very natural for the structure of Hamiltonian (7). (ii) *A priori*, this scheme represents a controllable approximation in the case of small v (large ε_a). (iii) For arbitrary values of parameters ε_a, ε_b and g, the ground state energy and the quasiparticle excitation energies obtained in the present framework turn out to be very close to those obtained with the help of the fully canonical transformation of Sec. VI C.

Transformation (A1)–(A3) minimizes the energy of the system when

$$u = \left(\frac{1}{2} + \frac{\mathrm{sign}(X)}{2} \sqrt{\frac{1 + \dfrac{Y^2}{Z^2}}{1 + \dfrac{Z^2}{X^2}}} \right)^{1/2}, \tag{A6}$$

$$v = \frac{1}{2}\left(\frac{1}{2} - \frac{\mathrm{sign}(X)}{2} \sqrt{\frac{1 + \dfrac{Y^2}{Z^2}}{1 + \dfrac{Z^2}{X^2}}} \right)^{1/2}, \tag{A7}$$

$$s = \left(\frac{1}{2} + \frac{\mathrm{sign}(Y)}{2} \sqrt{\frac{1 + \dfrac{X^2}{Z^2}}{1 + \dfrac{Z^2}{Y^2}}} \right)^{1/2}, \tag{A8}$$

$$w = -\left(\frac{1}{2} - \frac{\mathrm{sign}(Y)}{2} \sqrt{\frac{1 + \dfrac{X^2}{Z^2}}{1 + \dfrac{Z^2}{Y^2}}} \right)^{1/2}, \tag{A9}$$

where

$$X = \varepsilon_a(1 - 2n_A), \tag{A10}$$

$$Y = 4\varepsilon_b(1 - 2n_B), \tag{A11}$$

$$Z = g(1 - 2n_A)(1 - 2n_B). \tag{A12}$$

Here n_A and n_B are the occupation numbers of the quasiparticle states described by operators A_i and $B_{ij,\sigma}$, respectively, i.e.,

$$n_A = \frac{1}{\exp\left(\dfrac{\varepsilon_A}{T}\right) + 1}, \tag{A13}$$

$$n_B = \frac{1}{\exp\left(\dfrac{\varepsilon_B}{T}\right) + 1}. \tag{A14}$$

In Eqs. (A13) and (A14), variables ε_A and ε_B are the energies of the respective quasiparticle states.

At $T=0$, the constraints $|u|<1$ and $|s|<1$ impose the following condition for the existence of the physical solution:

$$g \geqslant \sqrt{4|\varepsilon_a \varepsilon_b|}. \tag{A15}$$

This condition is satisfied for any nonzero value of g, when either $\varepsilon_a=0$ or $\varepsilon_b=0$.

In the rest of this appendix, I limit the calculations only to Cases IA and IIA (in the classification of Sec. VI B).

Case IA: $\varepsilon_b=0$, $\varepsilon_a \geqslant 0$.

Condition $\varepsilon_b=0$ implies that, according to Eqs. (A8) and (A9), $s=1/\sqrt{2}$ and $w=-1/\sqrt{2}$, both independent of temperature. The coefficients u and v given by Eqs. (A6) and (A7) with $Y=0$ have temperature-dependent values.

A natural sign convention for this case is $\varepsilon_A > 0$ and $\varepsilon_B < 0$, i.e., at $T=0$, $n_A=0$ and $n_B=1$.

One can then obtain the energies

$$\varepsilon_A = \sqrt{\varepsilon_a^2 + g^2(1-2n_B)^2} \tag{A16}$$

and

$$\varepsilon_B = \frac{g^2(1-2n_A)(1-2n_B)}{4\varepsilon_A} \tag{A17}$$

of A-and B-quasiparticles, respectively.

The zero-temperature value of ε_A following from Eq. (A16) coincides with that of the Van Hove singularity (50) characterizing the spectrum of the "canonical solution." The values of ε_B given by Eqs. (A17) and (39) for the two solutions are also close to each other.

The ground state energy in the present case can be evaluated as

$$E_{\mathrm{GS}} = -\frac{N}{2}\left[\sqrt{\varepsilon_a^2 + g^2} - \varepsilon_a\right]. \tag{A18}$$

If E_{GS} given by Eq. (A18) is compared with the ground state energy of the canonical solution [Eq. (40)], then the difference is never greater than 5%.

At finite temperatures, in order to obtain n_A, n_B, ε_A and ε_B one has to solve the system of equations (A13), (A14), (A16), and (A17) numerically. It is easy to find, however, that the above system of equations always has one trivial solution: $\varepsilon_A=\varepsilon_a$, $\varepsilon_B=0$ with n_A and n_B given by Eqs. (A13) and (18). The condition for the existence of the second, nontrivial, solution can be found analytically. This condition is: $T<T_c$, where the critical temperature T_c is the solution of Eq. (46). Thus the remarkable fact is that T_c obtained in the framework of the present noncanonical scheme reproduces the canonical result of Sec. VI C.

Case IIA: $\varepsilon_a=0$, $\varepsilon_b \geqslant 0$.

According to Eqs. (A6)–(A9), the condition $\varepsilon_a=0$ implies that $u=1/\sqrt{2}$ and $v=1/\sqrt{8}$, while s and w have temperature-dependent values.

The sign convention in this case is: $\varepsilon_A<0$, $\varepsilon_B>0$, i.e., at $T=0$, $n_A=1$ and $n_B=0$. The calculation now gives

$$\varepsilon_A = \frac{g^2(1-2n_A)(1-2n_B)}{4\varepsilon_B}, \tag{A19}$$

$$\varepsilon_B = \sqrt{\varepsilon_b^2 + \frac{1}{16}g^2(1-2n_A)^2}, \tag{A20}$$

$$E_{\mathrm{GS}} = -2N\left[\sqrt{\varepsilon_b^2 + \frac{1}{16}g^2} - \varepsilon_b\right]. \tag{A21}$$

The critical temperature in this case is again the same as obtained from the canonical solution, i.e., it is given by Eq. (63).

In summary: The noncanonical variational scheme based on Eqs. (A1)–(A3) predicts the same critical temperature as the canonical scheme of Sec. VI C. Furthermore, the noncanonical scheme predicts the ground state energy and the important tunneling characteristics within a few per cent from the canonical result. The only significant feature of the canonical solution missing in the noncanonical one is the absence of the gap in the spectrum of A-quasiparticles in Case II. A related conceptual detail is that the noncanonical scheme fails to predict the coherent dispersion $\varepsilon_A(\mathbf{k})$ of A-quasiparticles.

I conclude this appendix with the following comment:

In the present variational scheme one can easily find that neither the variational energy nor the excitation spectrum will change, if the phases of transformation (A1)–(A3) are modified in the following way:

$$a_i = uA_i + v\,\eta_i \sum_{j(i)} e^{i\varphi_{ij}} A_j^+, \tag{A22}$$

$$b_{ij,+} = sB_{ij,+} + we^{i\varphi_{ij}} B_{ij,-}^+, \tag{A23}$$

$$b_{ij,-} = sB_{ij,-} - we^{i\varphi_{ij}} B_{ij,+}^+, \tag{A24}$$

where phases φ_{ij} can be different for different pairs of indices i and j.

The freedom to vary phases φ_{ij} in Eqs. (A22)–(A24) is, at least in part, due to the fact that the parameter space of noncanonical transformations is larger than that of canonical ones. Therefore, one may try to choose phases in Eqs. (A22)–(A24) such that transformation (A22) becomes canonical. I have found, that, in this way (with the selection of phases shown later in Fig. 6), the next nearest neighbor anticommutation test described earlier in this appendix can, indeed, be satisfied. However, a similar test for the pairs of supercells separated by one common neighbor cannot be satisfied independently of the choice of phases φ_{ij}. Transformation (A22) cannot be made rigorously canonical, because it involves only the nearest neighbors. It is, however, possible to conform with the canonical anticommutation relations, if transformation (A22) is modified to include more remote neighbors. Such a canonical transformation is much easier to describe in k-space—subject of Sec. VI C. One can thus conclude that the coherent dispersion of A-quasiparticles in k-space is protected by the Fermi statistics.

From a different perspective, one can also observe that, in the canonical scheme, the nonintuitive combination of phases φ_α given by Eq. (42) minimizes the pairing amplitude between more remote neighbors, which leads to the maximum energy gain from the nearest neighbors interacting *via* the Hamiltonian (7).

APPENDIX B: MINIMIZATION OF ENERGIES (40) and (61) WITH RESPECT TO PHASES ϕ_α

The minimization procedure presented in this appendix is equally applicable to the total energy expressions both in Case I [Eq. (40)] and in Case II [Eq. (61)]. Below, in order to be specific, I focus on the expression (40). This expression can be considered as an implicit function of phases φ_α entering it through the dependence on a single function $|V(\mathbf{k})|^2$.

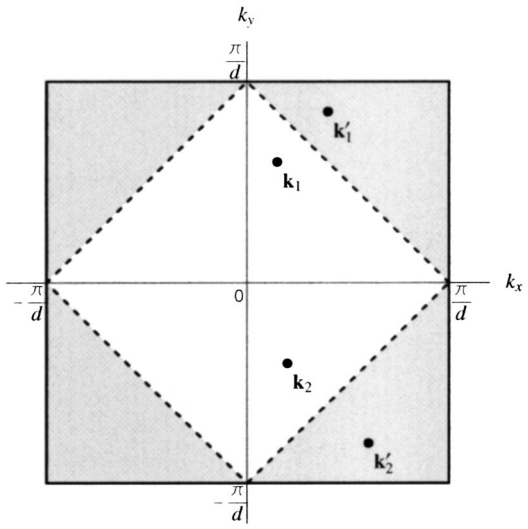

FIG. 17. Two examples of the pairs k points referred to in the text: $(\mathbf{k}_1,\mathbf{k}_1')$ and $(\mathbf{k}_2,\mathbf{k}_2')$. Thick solid lines represent the boundary of the first Brillouin zone of the stripe superstructure. The first k point of each pair should belong to the light region inside the dashed boundary. The second point should be obtained from the first one by reflection with respect to the nearest dashed line.

From Eq. (24)

$$|V(\mathbf{k})|^2 = 4\left\{\cos^2\left[\mathbf{kR}_1 + \frac{\varphi_1-\varphi_3}{2}\right] + \cos^2\left[\mathbf{kR}_2 + \frac{\varphi_2-\varphi_4}{2}\right] + 2\cos\left[\mathbf{kR}_1 + \frac{\varphi_1-\varphi_3}{2}\right] \times \cos\left[\mathbf{kR}_2 + \frac{\varphi_2-\varphi_4}{2}\right] \times \cos\left[\frac{\varphi_2+\varphi_4-\varphi_1-\varphi_3}{2}\right]\right\}. \quad \text{(B1)}$$

I first note that $|V(\mathbf{k})|^2$ is a periodic function of $\mathbf{k}$ in the directions of $\mathbf{R}_1$ and $\mathbf{R}_2$. Replacing sum in Eq. (40) by the integral according to the prescription (41), I further note that the symmetry of the function $|V(\mathbf{k})|^2$ is such, that any shift of the integration region does not change the value of the integral. Therefore, the result of the integration does not depend on the values of $\frac{\varphi_1-\varphi_3}{2}$ and $\frac{\varphi_2-\varphi_4}{2}$. In the following, in order to be specific, I choose $\frac{\varphi_1-\varphi_3}{2}=0$ and $\frac{\varphi_2-\varphi_4}{2}=0$.

The only phase combination to be constrained by the minimization of energy (40) is $\frac{\varphi_2+\varphi_4-\varphi_1-\varphi_3}{2}$. Now I switch back to the language of summation and note that the summation points in Eq. (40) can be divided in pairs $(\mathbf{k},\mathbf{k}')$ as shown in Fig. 17. Point $\mathbf{k}$ is chosen inside the white area surrounded by the dashed line, while $\mathbf{k}'$ is the nearest mirror image of $\mathbf{k}$ in the dark area outside of the dashed line. For each such a pair

$$|V(\mathbf{k})|^2 = 4[h(\mathbf{k}) + p(\mathbf{k})\zeta], \quad \text{(B2)}$$

while

$$|V(\mathbf{k}')|^2 = 4[h(\mathbf{k}) - p(\mathbf{k})\zeta], \quad \text{(B3)}$$

where

$$h(\mathbf{k}) = \cos^2[\mathbf{kR}_1] + \cos^2[\mathbf{kR}_2], \quad \text{(B4)}$$

$$p(\mathbf{k}) = 2\cos[\mathbf{kR}_1]\cos[\mathbf{kR}_2], \quad \text{(B5)}$$

$$\zeta = \cos\left[\frac{\varphi_2+\varphi_4-\varphi_1-\varphi_3}{2}\right]. \quad \text{(B6)}$$

Thus the energy (40) can be presented as

$$E = -\tilde{\sum_{\mathbf{k}}}\{F[h(\mathbf{k}) + p(\mathbf{k})\zeta] + F[h(\mathbf{k}) - p(\mathbf{k})\zeta]\}, \quad \text{(B7)}$$

where symbol "$\sim$" in the sum superscript implies that the summation is limited to the area shown in Fig. 17 inside the dashed line. Function F is implicitly defined by equation

$$F\left[\frac{1}{4}|V(\mathbf{k})|^2\right] = [1-2n_A(\mathbf{k})]\varepsilon_A(\mathbf{k}) - \varepsilon_a, \quad \text{(B8)}$$

where $\varepsilon_A(\mathbf{k})$ and $n_A(\mathbf{k}) \equiv n_A[\varepsilon_A(\mathbf{k})]$ are expressed as functions of $|V(\mathbf{k})|^2$ with the help of Eqs. (29) and (38). Even without specifying function F explicitly, one can take the derivative of E with respect to ζ to find

$$\frac{\partial E}{\partial \zeta} = -\tilde{\sum_{\mathbf{k}}} p(\mathbf{k})\left\{F'[h(\mathbf{k}) + p(\mathbf{k})\zeta] - F'[h(\mathbf{k}) - p(\mathbf{k})\zeta]\right\}, \quad \text{(B9)}$$

where F' is the first derivative of function F. Each term in the sum (B9) is equal to zero, when $\zeta=0$, which implies an extremum of E. I have examined a large number of examples numerically and have found that, in all cases considered, the above extremum corresponds to the global maximum. This result is also easy to derive analytically in the critical case by showing that all pairs of terms $F[h(\mathbf{k})+p(\mathbf{k})\zeta]+F[h(\mathbf{k})-p(\mathbf{k})\zeta]$ in Eq. (B7) simultaneously reach their maximal values, when $\zeta=0$.

Condition $\zeta=0$ substituted into Eq. (B6), then gives

$$\cos\left[\frac{\varphi_2+\varphi_4-\varphi_1-\varphi_3}{2}\right] = 0, \quad \text{(B10)}$$

from which Eq. (42) follows.

APPENDIX C: DERIVATION OF THE EQUATION FOR THE CRITICAL TEMPERATURE

In order to obtain the critical temperature in Case I of Sec. VI C, I substitute into Eq. (39) the limiting values of all quantities as $T-T_c \to 0_-$. In this limit

$$\varepsilon_A(\mathbf{k}) \to \varepsilon_a, \quad \text{(C1)}$$

$$n_A(\mathbf{k}) \to \frac{1}{\exp\left(\frac{\varepsilon_a}{T_c}\right)+1}. \quad \text{(C2)}$$

Simultaneously, $\varepsilon_B \to 0$, and $n_B \to 1/2$, i.e., $2n_B - 1 \to 0$. In order to resolve the uncertainty associated with substituting the limiting values of ε_B and $2n_B - 1$, it is necessary to keep the next order of ε_B in the expression for $2n_B - 1$, i.e.

$$2n_B - 1 \to -\frac{\varepsilon_B}{2T_c}. \tag{C3}$$

The substitution of Eqs. (C1)–(C3) into Eq. (39) leads to the following equation:

$$T_c = \frac{g^2\left[\exp\left(\frac{\varepsilon_a}{T_c}\right) - 1\right]}{16\varepsilon_a\left[\exp\left(\frac{\varepsilon_a}{T_c}\right) + 1\right]} \frac{1}{N}\sum_{\mathbf{k}} |V(\mathbf{k})|^2. \tag{C4}$$

Now I note, that, independently of the choice of phases in Eq. (B1),

$$\sum_{\mathbf{k}} |V(\mathbf{k})|^2 = 2N. \tag{C5}$$

The substitution of Eq. (C5) into Eq. (C4) then gives Eq. (46).

*Electronic address: fine@mpipks-dresden.mpg.de

[1] J. Zaanen and O. Gunnarsson, Phys. Rev. B **40**, 7391 (1989).
[2] D. Poilblanc and T. M. Rice, Phys. Rev. B **39**, 9749 (1989).
[3] H. J. Schulz, Phys. Rev. Lett. **64**, 1445 (1990).
[4] K. Machida, Physica C **158**, 192 (1989).
[5] M. Kato, K. Machida, H. Nakanishi, and M. Fujita, J. Phys. Soc. Jpn. **59**, 1047 (1990).
[6] S. R. White and D. J. Scalapino, Phys. Rev. B **61**, 6320 (2000).
[7] G. Seibold and J. Lorenzana, cond-mat/0307636.
[8] J. M. Tranquada, J. D. Axe, N. Ichikawa, Y. Nakamura, S. Uchida, and B. Nachumi, Phys. Rev. B **54**, 7489 (1996).
[9] H. A. Mook, P. Dai, F. Doğan, and R. D. Hunt, Nature (London) **404**, 729 (2000).
[10] E. W. Carlson, V. J. Emery, S. A. Kivelson, and D. Orgad, in *The Physics of Conventional and Unconventional Superconductors*, edited by K. H. Bennemann and J. B. Ketterson (Springer, Berlin, 2003), cond-mat/0206217.
[11] S. A. Kivelson, I. P. Bindloss, E. Fradkin, V. Oganesyan, J. M. Tranquada, A. Kapitulnik, and C. Howald, Rev. Mod. Phys. **75**, 1201 (2003).
[12] G. Seibold and M. Grilli, Phys. Rev. B **63**, 224505 (2001).
[13] J. M. Tranquada, N. Ichikawa, K. Kakurai, and S. Uchida, J. Phys. Chem. Solids **60**, 1019 (1999).
[14] D. S. Marshall, D. S. Dessau, A. G. Loeser, C. H. Park, A. Y. Matsuura, J. N. Eckstein, I. Bozovic, P. Fournier, A. Kapitulnik, W. E. Spicer, and Z.-X. Shen, Phys. Rev. Lett. **76**, 4841 (1996).
[15] A. Loeser, Z. X. Shen, D. S. Dessau, D. S. Marshall, C. H. Park, P. Fournier, and A. Kapitulnik, Science **273**, 325 (1996).
[16] H. Ding, T. Yukoya, J. C. Campuzano, T. Takahashi, M. Randeria, M. R. Norman, T. Mochiku, K. Hadowaki, and J. Giapintzakis, Nature (London) **382**, 51 (1996).
[17] A. Damascelli, Z. Hussain, and Z. X. Shen, Rev. Mod. Phys. **75**, 473 (2003).
[18] J. E. Hoffman, E. W. Hudson, K. M. Lang, V. Madhavan, H. Eisaki, S. Uchida, and J. C. Davis, Science **295**, 466 (2002).
[19] C. Howald, H. Eisaki, N. Kaneko, M. Greven, and A. Kapitulnik, Phys. Rev. B **67**, 014533 (2003).
[20] J. E. Hoffman, K. McElroy, D.-H. Lee, K. M. Lang, H. Eisaki, S. Uchida, and J. C. Davis, Science **297**, 1148 (2002).
[21] M. Vershinin, S. Misra, S. Ono, Y. Abe, Y. Ando, and A. Yazdani, Science **303**, 1995 (2004).
[22] A. Kapitulnik and G. Kotliar, Phys. Rev. Lett. **54**, 473 (1985).
[23] L. N. Bulaevskii and M. V. Sadovskii, J. Low Temp. Phys. **59**, 89 (1985).
[24] M. Ma and P. A. Lee, Phys. Rev. B **32**, 5658 (1985).
[25] B. Beschoten, S. Sadewasser, G. Güntherodt, and C. Quitmann, Phys. Rev. Lett. **77**, 1837 (1996).
[26] M. V. Sadovskii, Phys. Rep. **282**, 225 (1997).
[27] R. Micnas, S. Robaszkiewicz, and A. Bussmann-Holder, Phys. Rev. B **66**, 104516 (2002).
[28] E. Altman and A. Auerbach, Phys. Rev. B **65**, 104508 (2002).
[29] J. Ashkenazi, cond-mat/0308153.
[30] L. P. Gor'kov and A. V. Sokol, JETP Lett. **46**, 420 (1987).
[31] H. D. Chen, J. P. Hu, S. Capponi, E. Arrigoni, and S. C. Zhang, Phys. Rev. Lett. **89**, 137004 (2002).
[32] P. H. Hor and Y. H. Kim, J. Phys.: Condens. Matter **14**, 10377 (2002).
[33] P. Wrobel and R. Eder, Phys. Rev. B **62**, 4048 (2000).
[34] K. Yamada, C. H. Lee, K. Kurahashi, J. Wada, S. Wakimoto, S. Ueki, H. Kimura, Y. Endoh, S. Hosoya, G. Shirane, R. J. Birgeneau, M. Greven, M. A. Kastner, and Y. J. Kim, Phys. Rev. B **57**, 6165 (1998).
[35] H. A. Mook, P. Dai, S. M. Hayden, G. Aeppli, T. G. Perring, and F. Doğan, Nature (London) **395**, 580 (1998).
[36] M. Arai, T. Nishijima, Y. Endoh, T. Egami, S. Tajima, K. Tomimoto, Y. Shiohara, M. Takahashi, A. Garrett, and S. M. Bennington, Phys. Rev. Lett. **83**, 608 (1999).
[37] P. Dai, H. A. Mook, R. D. Hunt, and F. Doğan, Phys. Rev. B **63**, 054525 (2001).
[38] S. Wakimoto, R. J. Birgeneau, M. A. Kastner, Y. S. Lee, R. Erwin, P. M. Gehring, S. H. Lee, M. Fujita, K. Yamada, Y. Endoh, K. Hirota, and G. Shirane, Phys. Rev. B **61**, 3699 (2000).
[39] C. H. Chen, S.-W. Cheong, and A. S. Cooper, Phys. Rev. Lett. **71**, 2461 (1993).
[40] J. Li, Y. Zhu, J. M. Tranquada, K. Yamada, and D. J. Buttrey, Phys. Rev. B **67**, 012404 (2003).
[41] O. Zachar, S. A. Kivelson, and V. J. Emery, Phys. Rev. B **57**, 1422 (1998).
[42] C. Stock, W. J. L. Buyers, R. Liang, D. Peets, Z. Tun, D. Bonn, W. N. Hardy, and R. J. Birgeneau, Phys. Rev. B **69**, 014502 (2004).
[43] V. Hinkov, S. Pailhès, P. Bourges, Y. Sidis, A. Ivanov, A. Kula-

kov, C. T. Lin, D. P. Chen, C. Bernhard, and B. Keimer, Nature (London) (to be published).
[44] J. M. Tranquada, J. D. Axe, N. Ichikawa, A. R. Moodenbaugh, Y. Nakamura, and S. Uchida, Phys. Rev. Lett. **78**, 338 (1997).
[45] K. Hirota, K. Yamada, I. Tanaka, and H. Kojima, Physica B **241–243**, 817 (1998).
[46] H. Kimura, K. Hirota, H. Matsushita, K. Yamada, Y. Endoh, S. Lee, C. F. Majkrzak, R. Erwin, G. Shirane, M. Greven, Y. S. Lee, M. A. Kastner, and R. J. Birgeneau, Phys. Rev. B **59**, 6517 (1999).
[47] K. Hirota, Physica C **357–360**, 61 (2001).
[48] M. Fujita, H. Goka, K. Yamada, and M. Matsuda, Phys. Rev. Lett. **88**, 167008 (2002).
[49] A. J. Leggett, Rev. Mod. Phys. **47**, 331 (1975).
[50] E. M. Lifshitz and L. P. Pitaevskii, *Statistical Physics 2. Theory of the Condensed State* (Pergamon, Oxford, 1996).
[51] C. Bernhard, J. L. Tallon, Th. Blasius, A. Golnik, and Ch. Niedermayer, Phys. Rev. Lett. **86**, 1614 (2001).
[52] J. W. Loram, J. Luo, J. R. Cooper, W. Y. Liang, and J. L. Tallon, J. Phys. Chem. Solids **62**, 59 (2001).
[53] J. L. Tallon, J. W. Loram, J. R. Cooper, C. Panagopoulos, and C. Bernhard, Phys. Rev. B **68**, 180501 (2003).
[54] S. H. Pan, E. W. Hudson, A. K. Gupta, K. W. Ng, H. Eisaki, S. Uchida, and J. C. Davis, Phys. Rev. Lett. **85**, 1536 (2000).
[55] Ch. Renner and Ø. Fischer, Phys. Rev. B **51**, 9208 (1995).
[56] R. Koltun, M. Hoffmann, P. C. Splittgerber-Hünnekes, Ch. Jarchow, G. Güntherodt, V. V. Moshchalkov, and L. I. Leonyuk, Z. Phys. B: Condens. Matter **82**, 53 (1991).
[57] Figure 8 of Ref. 56 contains a strongly asymmetric point-contact tunneling spectrum characterized by $\Delta/T_c=6.8$, where Δ is obtained as the half of the peak-to-peak separation. Citing Ref. 56, I imply the above ratio for that spectrum. However, the authors of Ref. 56 have assumed that they accidentally measured an SIS contact and, therefore, listed Δ equal to the quater of the peak-to-peak separation.
[58] Y. DeWilde, N. Miyakawa, P. Guptasarma, M. Iavarone, L. Ozyuzer, J. F. Zasadzinski, P. Romano, D. G. Hinks, C. Kendziora, G. W. Crabtree, and K. E. Gray, Phys. Rev. Lett. **80**, 153 (1998).
[59] Ch. Renner, B. Revaz, J.-Y. Genoud, K. Kadowaki, and Ø. Fischer, Phys. Rev. Lett. **80**, 149 (1998).
[60] Ch. Renner, B. Revaz, K. Kadowaki, I. Maggio-Aprile, and Ø. Fischer, Phys. Rev. Lett. **80**, 3606 (1998).
[61] S. Misra, S. Oh, D. J. Hornbaker, T. DiLuccio, J. N. Eckstein, and A. Yazdani, Phys. Rev. Lett. **89**, 087002 (2002).
[62] K. McElroy, D.-H. Lee, J. E. Hoffman, K. M. Lang, E. W. Hudson, H. Eisaki, S. Uchida, J. Lee, and J. C. Davis, cond-mat/0404005.
[63] J. Y. T. Wei, C. C. Tsuei, P. J. M. van Bentum, Q. Xiong, C. W. Chu, and M. K. Wu, Phys. Rev. B **57**, 3650 (1998).
[64] J. Chen, J. F. Zasadzinski, K. E. Gray, J. L. Wagner, and D. G. Hinks, Phys. Rev. B **49**, 3683 (1994).
[65] G. T. Jeong, J. I. Kye, S. H. Chun, S. Lee, S. I. Lee, and Z. G. Khim, Phys. Rev. B **49**, 15 416 (1994).
[66] L. Ozyuzer, Z. Yusof, J. F. Zasadzinski, R. Mogilevsky, D. G. Hinks, and K. E. Gray, Phys. Rev. B **57**, 3245 (1998).
[67] Q. Huang, J. F. Zasadzinski, K. E. Gray, J. Z. Liu, and H. Claus, Phys. Rev. B **40**, 9366 (1989).
[68] I. Maggio-Aprile, Ch. Renner, A. Erb, E. Walker, and Ø. Fischer, Phys. Rev. Lett. **75**, 2754 (1995).
[69] Q. Huang, J. F. Zasadzinski, K. E. Gray, E. D. Bukowski, and D. M. Ginsberg, Physica C **161**, 141 (1989).
[70] H. Murakami and R. Aoki, J. Phys. Soc. Jpn. **64**, 1287 (1994).
[71] H. Murakami, S. Ohbuchi, and R. Aoki, J. Phys. Soc. Jpn. **63**, 2653 (1994).
[72] N. Miyakawa, P. Guptasarma, J. F. Zasadzinski, D. G. Hinks, and K. E. Gray, Phys. Rev. Lett. **80**, 157 (1998).
[73] M. Suzuki and T. Watanabe, Phys. Rev. Lett. **85**, 4787 (2000).
[74] V. M. Krasnov, Phys. Rev. B **65**, 140504 (2002).
[75] Y. Yamada, K. Anagawa, T. Shibauchi, T. Fujii, T. Watanabe, A. Matsuda, and M. Suzuki, Phys. Rev. B **68**, 054533 (2003).
[76] S. I. Vedeneev, A. G. M. Jansen, P. Samuely, V. A. Stepanov, A. A. Tsvetkov, and P. Wyder, Phys. Rev. B **49**, 9823 (1994).
[77] V. M. Krasnov, Physica C **372–376**, 103 (2002).
[78] J. X. Zhu, I. Martin, and A. R. Bishop, Phys. Rev. Lett. **89**, 067003 (2002).
[79] A. Polkovnikov, M. Vojta, and S. Sachdev, Phys. Rev. B **65**, 220509 (2002).
[80] Q. H. Wang and D. H. Lee, Phys. Rev. B **67**, 020511 (2003).
[81] A. S. Alexandrov, J. Supercond. **17**, 53 (2003).
[82] H. D. Chen, O. Vafek, A. Yazdani, and S. C. Zhang, cond-mat/0402323.
[83] Y. J. Uemura, A. Keren, L. P. Le, G. M. Luke, W. D. Wu, Y. Kubo, T. Manako, Y. Shimakawa, M. Subramanian, J. L. Cobb, and J. T. Markert, Nature (London) **364**, 605 (1993).
[84] Ch. Niedermayer, C. Bernhard, U. Binninger, H. Glückler, J. L. Tallon, E. J. Ansaldo, and J. I. Budnick, Phys. Rev. Lett. **71**, 1764 (1993).
[85] C. Bernhard, Ch. Niedermayer, U. Binninger, A. Hofer, Ch. Wenger, J. L. Tallon, G. V. M. Williams, E. J. Ansaldo, J. Budnick, C. E. Stronach, D. R. Noakes, and M. A. Blankson-Mills, Phys. Rev. B **52**, 10 488 (1995).
[86] C. Panagopoulos, B. D. Rainford, J. R. Cooper, W. Lo, J. L. Tallon, J. W. Loram, J. Betouras, Y. S. Wang, and C. W. Chu, Phys. Rev. B **60**, 14 617 (1999).
[87] Y. J. Uemura *et al.*, Phys. Rev. Lett. **62**, 2317 (1989).
[88] T. Pereg-Barnea, P. J. Turner, R. Harris, G. K. Mullins, J. S. Bobowski, M. Raudsepp, R. Liang, D. A. Bonn, and W. N. Hardy, cond-mat/0311555 (2003).
[89] Ya. G. Ponomarev *et al.*, Phys. Rev. B **52**, 1352 (1995).
[90] Ya. G. Ponomarev *et al.*, Physica C **243**, 167 (1995).
[91] J. F. Zasadzinski, L. Ozyuzer, N. Miyakawa, K. E. Gray, D. G. Hinks, and C. Kendziora, Phys. Rev. Lett. **87**, 67005 (2001).
[92] L. Buschmann, M. Boekholt, and G. Güntherodt, Physica C **203**, 68 (1992).
[93] Q. Chen, K.-W. Ng, A. E. Manzi, and H. L. Luo, Phys. Rev. B **49**, 6193 (1994).
[94] J. F. Annett, N. Goldenfeld, and A. J. Leggett, in *Physical Properties of High Temperature Superconductors*, edited by D. M. Ginsberg (World Scientific, Singapore, 1996), Vol. 5, p. 375, cond-mat/9601060.
[95] D. A. Wollman, D. J. Van Harlingen, W. C. Lee, D. M. Ginsberg, and A. J. Leggett, Phys. Rev. Lett. **71**, 2134 (1993).
[96] C. C. Tsuei, J. R. Kirtley, C. C. Chi, L. S. Yu-Jahnes, A. Gupta, T. Shaw, J. Z. Sun, and M. B. Ketchen, Phys. Rev. Lett. **73**, 593 (1994).
[97] C. C. Tsuei, J. R. Kirtley, G. Hammerl, J. Mannhart, H. Raffy, and Z. Z. Li, cond-mat/0402655.
[98] A. G. Sun, D. A. Gajewski, M. B. Maple, and R. C. Dynes, Phys. Rev. Lett. **72**, 2267 (1994).